Cross Borehole Induced Polarization to Detect Subsurface NAPL at the Savannah River Site, South Carolina

by

Michael B. Lambert

B.S., Geology and Geophysics (2002)

University of Connecticut

Submitted to the Department of Earth, Atmospheric
and Planetary Sciences in Partial Fulfillment for
the Master of Science in Geosystems

at the

Massachusetts Institute of Technology

May 2003

© 2003 Massachusetts Institute of Technology
All Rights Reserved.

Signature of Author ....
Earth, Atmospheric and Planetary Sciences
May 19 2003

Certified by ....
F. Dale Morgan
Professor
Thesis Advisor

Accepted by ....
Ronald G. Prinn
Chairman, Department Committee on Graduate Students

MASSACHUSETTS INSTITUTE
OF TECHNOLOGY
SEP [illegible] 2003
LIBRARIES

WITHDRAWN
FROM
MIT LIBRARIES

LINDGREN

Abstract

Spectral induced polarization measurements were acquired in six cross-borehole panels within four boreholes at the Savannah River Site. The investigation was performed to delineate the presence of dense non-aqueous phase liquids (DNAPL) which were periodically released from the 1950's through the 1980's at the A-14. Measurements were made at 1/4 and 1/16 Hertz and the first four odd harmonics. Data inversion for model parameters was performed with the use of proprietary Earth Resources Laboratory inversion codes. Results indicate the possible presence of three main zones of contamination within the region of our wells. Based on the geophysical results, suggestions have been made regarding the location of three wells to be used for ground truthing.

Table of Contents

Acknowledgements

I would like to thank Victoria Briggs for time and efforts in electrode design and construction and also Burke Minsley for electrode design and construction and field assistance. John Sogade was extremely helpful in assistance with virtually all aspects of this project including electrode design and construction, field assistance, troubleshooting inverse codes and for answering many questions I've had throughout the project. I am indebted to my advisor Dale Morgan for his support and guidance throughout the year and for giving me such a fantastic project.

1. Introduction

Geophysics in Contamination Investigations

Spectral induced polarization (SIP) is the measurement of induced polarization (IP) within a six decade frequency range from .001 to 1,000 Hz. IP is a delayed voltage response of subsurface material in the presence of applied currents. The effect arises due to current resisting chemical reactions which occur at the boundaries of pore solution with both metallic minerals and clay particles. These effects are altered when other materials such as chemical contaminants are introduced into pore spaces. IP is a promising geophysical method because it has a unique sensitivity to lithologic variability and the surface properties of subsurface materials (Lesmes and Frye, 2001). Much laboratory work has been done to show the effects of contaminants on the IP response; however, the theoretical aspects of the science are not entirely understood. This study works to develop a methodology that can be applied to use SIP for mapping contaminant distribution through a field example from the Savannah River Site.

Geophysical methods have been widely used in subsurface contamination investigations. The ability to obtain a clear and correct image of the subsurface is paramount for the design and implementation of proper remediation schemes and assessment of the impact that contamination might have on local ecosystems and groundwater supplies. Many types of geophysical methods have been used in past studies including: ground penetrating radar (GPR) (Olhoeft, 1992, Lane and others, 2000), two-dimensional earth resistivity (Powers and others, 1999), electromagnetic induction (Johnson and others, 2002b), and several borehole logging methods (Johnson and others, 2002a, Williams and Others, 2002). Success has been attained in many cases when appropriate data processing and inversion algorithms are employed and the choice of geophysical method is appropriate considering the earth material properties, type of contamination and estimation of cultural artifacts that may affect geophysical measurements. Given the many constraints, it is important that geophysical invention and innovation prosper as the field moves into the future. The usefulness of geophysical methods for contamination investigations lies entirely within their ability to detect contamination plumes of all kinds, accurately resolve their size and distribution and possibly give a rough assessment of the type of contaminants located in the subsurface.

A-14 Outfall Description

The A-14 outfall was historically used as a disposal site for chlorinated solvents, including Tetrachloroethylene (PCE) and Trichloroethylene (TCE). An estimated 1.5 million pounds have been released from the 1950's through the early 1980's (Jackson et al., 1999). Approximately 72% of this effluent was PCE and 27% TCE, with trace amounts of 1,1,1 Trichloroethane. Since the mid 1980's many site characterization efforts have taken place at the A-14, including: exploratory/monitoring wells, geologic/lithologic investigations, cone penetrometry, ribbon NAPL sampling, soil vapor extraction etc. Although the results of most of these chemical studies are not available, geological logs and contaminant depth profiles from the MVE series of wells were provided in Jackson et al. (1999). The area is predominantly sand and clay with intermittent fine grained and silty-clay regions. A thick sand/sand-mix layer is pervasive throughout the entire site at depths of 20 to 45 feet. This structure suggests that contaminants may be heterogeneously distributed throughout the region most likely nesting in areas of higher porosity and permeability such as sand units (Morgan, 2001).

Figure 1.1 is plan map of the A-14 showing the location of the MIT series of wells used in this study in relation to older wells from the MVE, MES, HFM and MRS series. The MIT series is located north of the previous wells, closer to the sewer pipe where contaminants were released. Previous studies have indicated that contamination may not have traveled as far south as originally estimated and sufficient TCE and PCE concentration should be located at shallow depths within the region of MIT wells (Vangelas, 2000). The average water table depth at the A-14 exceeds 100 feet while the MIT wells reach a maximum of 80 feet in depth. This limits the spectral IP characterization to contaminants within the vadose zone where soil vapor extraction has effectively removed 166,100 pounds of chlorinated solvent throughout the entire A-14.

PCE profiles of the MVE well series from Jackson et al. (2000) were used to construct figure 1.2, a contour map of PCE and TCE concentrations at a depth of 9 meters. This map is useful gain a rough idea of the contaminant distribution within the MVE well series. Concentrations are in parts per million by volume on a logarithmic scale, for example a concentration of 2 is 100 ppmv. PCE is present in all holes at a minimum depth of 15 to 20 feet, and a maximum depth of 40 to 65 feet. Well MVE-13 is closest to the MIT series of wells, specifically that of MIT-3. If the earth is relatively homogeneous over this short distance then we might expect PCE to affect the spectral IP response as MVE-13 has concentrations ranging from 100 to 1000 ppmv. Wells MVE-14 and MVE-15, which have low concentrations of PCE, are also within close proximity to the west of the MIT series. This suggests that lateral contaminant movement is minimal within the MIT series and we may expect the contaminant plume to strike north-south within this region. A plume of this shape is advantageous because all MIT boreholes do not contain very high concentrations of contaminant and SIP will be able to correctly identify the contaminant signature relative to the minimally contaminated background.

Thesis Objectives

The objective of this thesis is to develop a methodology by which SIP can be used for the mapping of contaminant distribution when implemented in a cross-borehole fashion. This objective is carried out through the following sub-sections: [1] the development of equipment which are most applicable to a study of this nature, [2] the refinement of field setup and data collection schemes so as to limit the amount of noise introduced into data, [3] the use of data processing and inversion algorithms that identify useful data and calculate accurate models from this data, and [4] the correct interpretation of inverted models within the context of supplementary information in an effort to discriminate between contaminant anomalies and other structural/cultural noise sources.

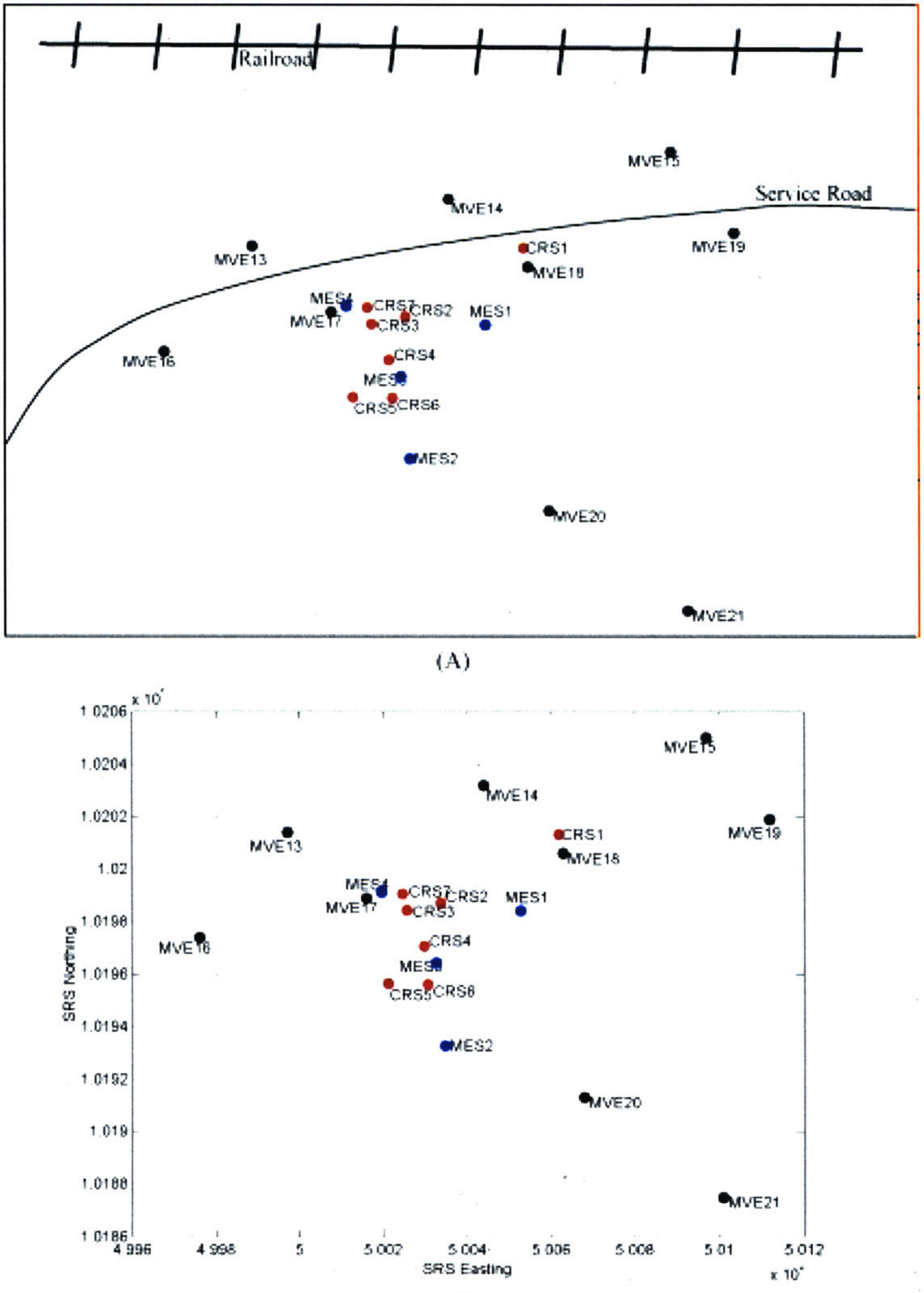

(A)

(B)

Figure 1.1 – Rough map (A) of the A-14 outfall and scaled map (B) using SRS coordinate convention. Both maps show historic wells and MIT wells used in this study.

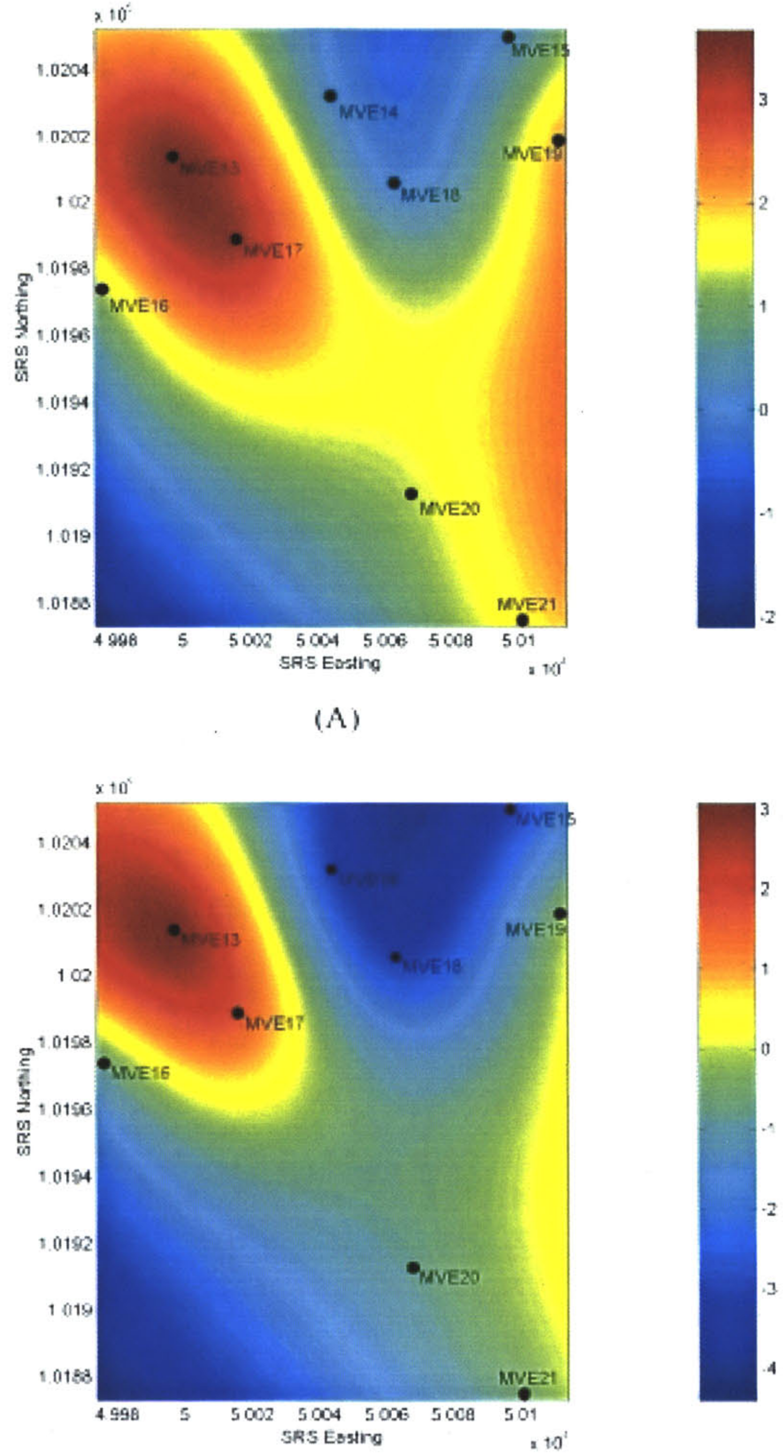

(A)

(B)

Figure 1.2 – Concentration of PCE (A) and TCE (B) at a depth of 9 meters within the MVE well series. Values are in parts per million by volume (ppmv) on a base 10 logarithmic scale. Data used from Jackson et al. (2000)

2. Data Processing

Organization and Processing

Data output from the receiver is in a very obscure and awkward format, a matlab script was written to convert data into a more useful format. Conversion of voltage and phase to real and imaginary impedance allowed for each of the panels to be re-referenced. This was necessary because all potential measurements were made relative to the top electrode in borehole MIT-1, referred to as the universal electrode. In order to invert data as two-dimensional panels the data had to be referenced to an electrode within that panel, this required subtracting all impedance values within the borehole from the impedance value of the new reference against the universal reference. In situations where re-referencing was necessary, the new reference electrode was the first usable potential electrode within the lower numbered borehole. Some electrodes were not usable as references because their measurement against the universal reference was poor and the data point was filtered out.

Bad data points are very prevalent in induced polarization surveys and occur for many reasons. Sources of noise include, EM coupling, capacitive coupling, streaming potentials, telluric potentials, metallic minerals, malfunctioning equipment and cultural artifacts such as power lines and buried objects. Removing poor data is a necessity if correct inverted models are expected. The simple criterion used is based on the quadrant in which the measured data plots in. Because we are interested in the capacitive effects of the earth, current is expected to lag behind voltage inducing a negative phase. This can be seen in phase values that plot in the second and fourth quadrants. All other data points are removed. Figure 3.1 is a table displaying the number of useful data points out of the 819 collected for each panel at the ten different frequencies. This is a first order of approximation of how noise varies with frequency, though it should not be taken as a measure of the noise. Please also note that the scarcity of useful data at the two highest frequencies of panel five are hardly normal and represent other issues perhaps caused by equipment problems.

Data Inversion

Inverting geophysical data for model parameters is a very important aspect of using geophysics for subsurface contamination investigations. Inversion accuracy is defined by how well the location and value of one or more anomalies are resolved. If either is incorrect the inferred subsurface structure is wrongly interpreted undermining the overall goal of the investigation.

The Earth Resources Laboratory has developed modeling and inversion codes which are fast, accurate and stable. They use finite difference and the bi-conjugate gradient method for both the forward and inverse algorithms. The fundamental equation is Ohm's law, for our interest given by

$$\nabla(\sigma(\underline{x})\nabla V(\underline{x})) = -I(\underline{x})$$

where:

$\underline{x}$ = *position vector*
σ = *conductivity*
V = *voltage*
I = *current*

Stability and accuracy is achieved in the inversion algorithm by the use of Tikhonov regularization. The objective function Ψ(m), which is minimized is:

$$\Psi(\underline{m}) = \left\| \underline{d} - \underline{G}(\underline{m}) \right\|^2 + \tau \left\| \nabla^2 \underline{m} \right\|^2$$

where:

$\underline{d}$ = *data*
$\underline{G}$ = *model*
τ = *regularization parameter*
$\underline{m}$ = *model parameter*

In model space the cross-borehole panel consists of 14 vertical model blocks, with a fixed spacing of six meters, and eight horizontal blocks whose size depends on the distance between the two boreholes. Model blocks are also placed to the left right and bottom of the panel, these 'padding' blocks and 'boundary' blocks are necessary to sustain the boundary conditions of the problem. Typically the six padding blocks are the same size as model blocks within the panel, while the two boundary blocks are ten and 100 times larger than model blocks in their respective dimension. Figure 3.4 shows the entire model space the panel including the location of the 15 electrodes, also referred to as nodes.

		.25 Hertz	.0626 Hertz
Panel 1-3	fundamental	793	797
	1st harmonic	766	800
	2nd harmonic	755	797
	3rd harmonic	746	424
	4th harmonic	706	416
Panel 1-3	fundamental	730	721
	1st harmonic	710	670
	2nd harmonic	699	645
	3rd harmonic	696	635
	4th harmonic	679	629
Panel 1-4	fundamental	765	761
	1st harmonic	724	770
	2nd harmonic	711	767
	3rd harmonic	703	759
	4th harmonic	695	743
Panel 2-3	fundamental	710	692
	1st harmonic	709	718
	2nd harmonic	695	731
	3rd harmonic	687	732
	4th harmonic	682	728
Panel 2-4	fundamental	770	796
	1st harmonic	768	793
	2nd harmonic	767	790
	3rd harmonic	~150	~150
	4th harmonic	~150	~150
Panel 3-4	fundamental	729	734
	1st harmonic	760	764
	2nd harmonic	754	773
	3rd harmonic	728	360
	4th harmonic	689	338

Figure 3.1 – Number of good data points per panel at each frequency out of 819 total data points per panel.

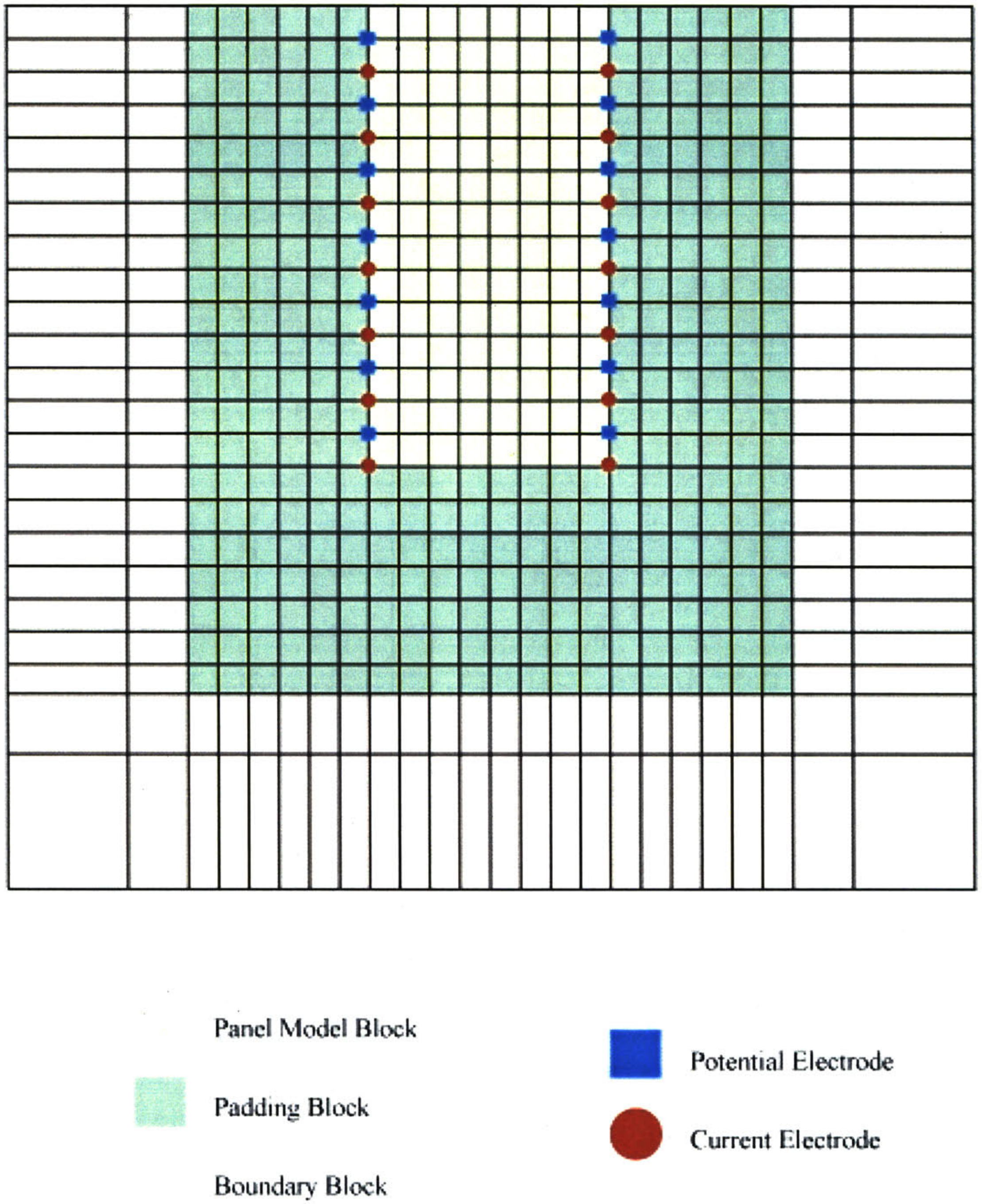

Figure 3.2 – Schematic diagram of blocks which make up the model space. Padding and boundary blocks are used to sustain the boundary conditions of the model.

3. Induced Polarization Theory

Induced polarization is the presence of a delayed voltage response in earth materials (Sumner, 1976). The delayed voltage response can be interpreted as the earth's ability to store charge, similar to a capacitor. Two physical processes have been attributed to the polarizing effects under an applied electrical current, (1) the interface chemistry of a metallic mineral and pore solution (electrode polarization) and (2) the interface chemistry of a non-metal and pore solution (membrane polarization). Current termination leads to relaxation of the polarized interfaces which is observed as a time dependent voltage decay. Within the frequency domain a spectral response is observed because polarization effects are a function of the frequency of the applied current (Ward, 1990). Surface chemical properties of subsurface materials dominate the extent to which membrane and electrode polarization occur (Lesmes and Frye, 2001), and are drastically altered by the presence of contamination. Laboratory and field investigations have verified the spectral response of IP to the presence of contamination for many different contaminants and lithologies (Vanhala et al., 1992, Olhoeft, 1992).

Time domain induced polarization consists of measuring the voltage response to injection of a square wave current. Figure 4.1 is an example of the transmitted and received waveforms. Measurement of earth response is calculated through the integration of the decaying voltage, known as chargeability (M)

$$M = \frac{\int_{t_s}^{t_f} V_s\,dt}{V_p} \frac{1}{\Delta t}$$

where:

Vs = decaying voltage
Vp = signal voltage measured during current application
Ts = beginning of measured time window, after current termination
Tf = end of measured time window
Δt = *length of time window.*

Time domain measurements are related to frequency domain through the Fourier transform. Practically speaking, however, measurements are much too crude to allow a unique transformation.

Within the frequency domain several measures can be used to characterize the polarization of the subsurface. The percent frequency effect (PFE) is a measure of the increase in conductance across several decades of frequency (Madden and Cantwell, 1959), in terms of resistivity the PFE is given by

$$PFE = \frac{\rho_{dc} - \rho_{ac}}{\rho_{ac}} \times 100\%$$

where:

ρ_{dc} = *very low frequency alternating current*
ρ_{ac} = *alternating current at higher frequency.*

The metal conduction factor (MCF) can be derived from the PFE by multiplying through the ac conductivity of the medium resulting in a measurement of the conductivity of blocked paths. MCF is most applicable when searching for metallic mineralsbut may be used to discriminate between metal and non-metal targets (Madden and Cantwell, 1959). Phase may also be measured in the frequency domain and represents the shift between output current and input voltage as a result of polarization effects. Phase is simply calculated by

$$\phi = \tan^{-1}\left(\frac{Z_{im}}{Z_{re}}\right)$$

where:

$Z_{im} = imaginary\ impedance = \frac{V}{I}\cos\phi$

$Z_{re} = real\ impedance = \frac{V}{I}\sin\phi.$

Generally speaking, the physical phenomenon that determine measured chargeability, PFE, MCF and phase values can be broken down into two parts. A real bulk material resistivity term and a complex surface resistivity term. The magnitude of the real term is much larger as it constitutes the large scale resistance determined by electrolytic pathways. Conversely the complex term is small in magnitude, however constitutes the entire IP effect because it relates to the method of polarization, electrode or membrane, and the chemical, geometrical and physical properties of pore paths under. A more rigorous treatment may be found in Lesmes and Frye (2001), Marshall and Madden, (1959).

Electrode Polarization

The presence of metallic minerals blocking pore paths of subsurface materials leads to the electrode polarization effect. Electrical current reaches the solution/metal interface through ion movement and a chemical reaction is required pass current through this boundary. Depending on the type of mineral and chemical constituents within the pore solution, only a percentage of the present ions will partake in this reaction. This ion selective membrane causes ion concentrated and deficient regions within the pore path which is polarization. Termination of the current relaxes ions and gradients return to equilibrium states. The resulting impedance at this boundary is referred to as the Warburg impedance and is proportional to the frequency raised to the negative one-half power within the frequency range of interest. The surface resistivity term described above is dependent on metal concentration, metal distribution and the type of metals present.

At higher frequencies than what SIP utilizes, other effects can be a factor in electrode polarization including the effective capacitance of the adsorbed layer of ions on the particle surface. The analogous electrical circuit for electrode polarization is shown in figure 4.2, the spectral impedance response of this circuit is the generalized Cole-Cole model (Pelton et al., 1978).

Membrane Polarization

Similarly to electrode polarization, membrane polarization is caused by the presence of a charged particle within a pore path. In an equilibrium state, negatively charged particles, such as clay, attract positive ions in the pore solution forming a cation cloud within the pore path. Application of current causes ion concentrated regions as more cations move into the cloud, which oppose the flow of current (Ward, 1990). This effect is most pronounced at lower frequencies around .01 Hz and does not occur for frequencies higher than 1000 Hz. The distance to which the cation cloud extends into the pore path is given by

$$d = \frac{K_e k T}{\sqrt{2 n e^2 v^2}}$$

where:

n = normal ion concentration of electrolyte
v = valence of normal ions
e = elementary charge
Ke = relative dielectric permittivity of the fluid medium
K = Boltzman's constant
T = temperature.

In the presence of contamination d can change very much through changes in the dielectric constant and ion concentration.

When membrane polarization is the dominant IP effect the surface conduction term is directly related to d. Physical properties of clay particles such as specific surface area, cation exchange capacity and surface charge density affect the surface conduction term, hence they affect d.

Capacitive and Electromagnetic Coupling

IP field measurements are hindered by two main coupling problems which appear as noise within measured data. In many situations proper care can be taken to remove certain aspects of coupling, however these options are limited when electrodes are deployed in boreholes. Both inductive and capacitive coupling are understood quite well theoretically although application of corrective algorithms is still tricky because it requires accurate assessment the same subsurface properties that IP is intending to measure.

Capacitive coupling manifests itself through three paths, [1] leakage current from the transmitting wire that is picked up at the receiving electrode, [2] current from the transmitting electrode that is picked up by the receiving wire and [3] current that leaks directly from wire to wire. The magnitudes of the first two effects are small enough so that they will not affect our measurements. However,for borehole measurements the third capacitive coupling method is of serious concern because of the close proximity of wires within the borehole. Using a modified formulation of the model described in Waite (1959) as we have no grounding shield,

$$Z_{coupling} = \frac{R_1 R_3}{R_1 + R_3 - \frac{i}{\omega C}}$$

where:

R_1 = *transmitting electrode resistance*
R_3 = *receiving electrode resistance*
ω = *angular frequency of transmitted current*
C = *capacitance between transmitting and receiving wire*
$i^2 = -1$.

R_1 and R_3 have been measured in the laboratory, C is a function of subsurface material properties, wire radius and the distance between the wires. Refer to figure 4.3 for a schematic and equivalent circuit of capacitive coupling. The impedance due to capcitive coupling is equal to the impedance across R_3. Lab measurements of our equipment yield a value of $3.7 \times 10^{-7} + .0059i$. This is approximately one order of magnitude less than the average measured voltage, however measurements in the microvolt range will be seriously affected.

Electromagnetic (inductive) coupling is the mutual inductive impedance between transmitting and receiving electrodes. The effects of EM coupling can drown out signals within the frequency range of interest but are largest at 30,000 Hz (Vandiver, 1998). Because EM coupling occurs through the propagation of electromagnetic waves, the presence of a highly conductive subsurface only serves to enhance the effect. Solutions to the problem have been presented in the cases of collinear arrays over homogeneous and two-layer half spaces and are quite complicated. Formulation of the problem within the borehole framework is not readily available and is not included within the scope of this project; a rigourous treatment of the subject can be found in Millet (1967).

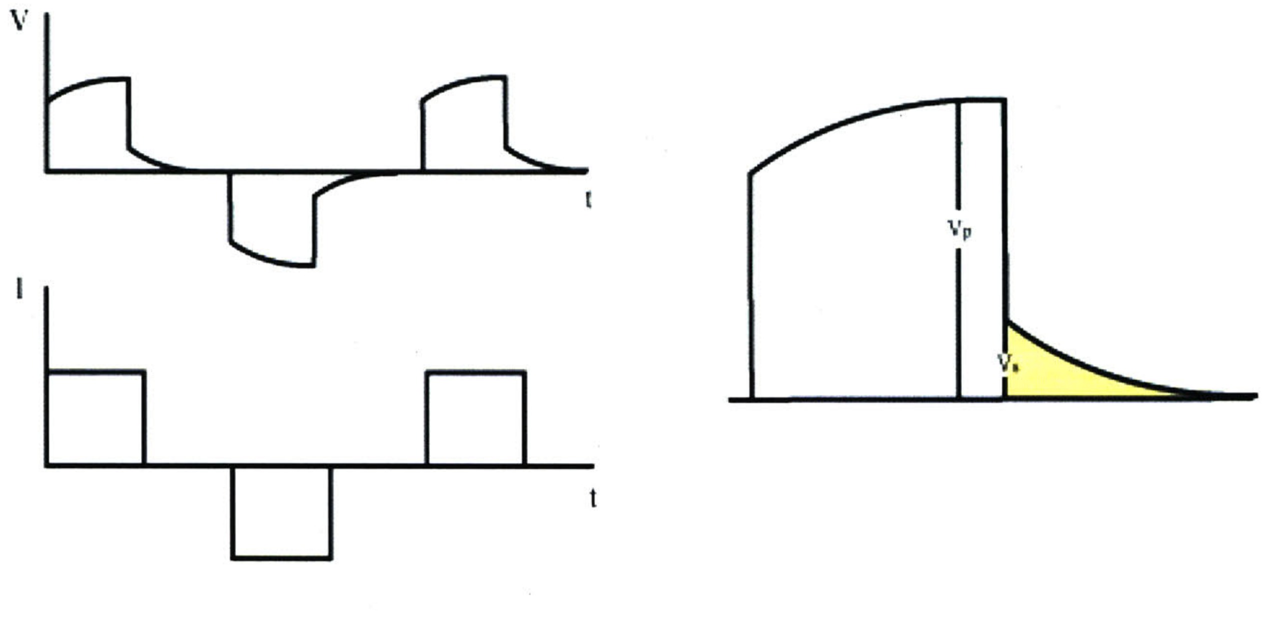

(A) (B)

Figure 4.1 – Square wave current input and voltage response shown in (A), polarization is seen at the top of the voltage waveform. Voltage signal in (B), yellow shaded area is measured chargeability.

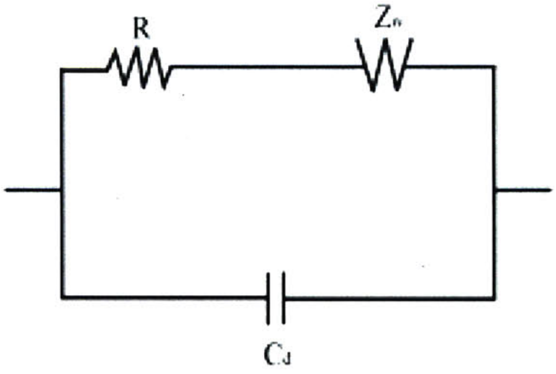

Figure 4.2 – Equivalent circuit of electrode polarization. Impedance is calculated from this circuit using the Cole-Cole model. Z_w is the Warburg impedance which is the effect most prevalent at the frequencies at which IP is measured.

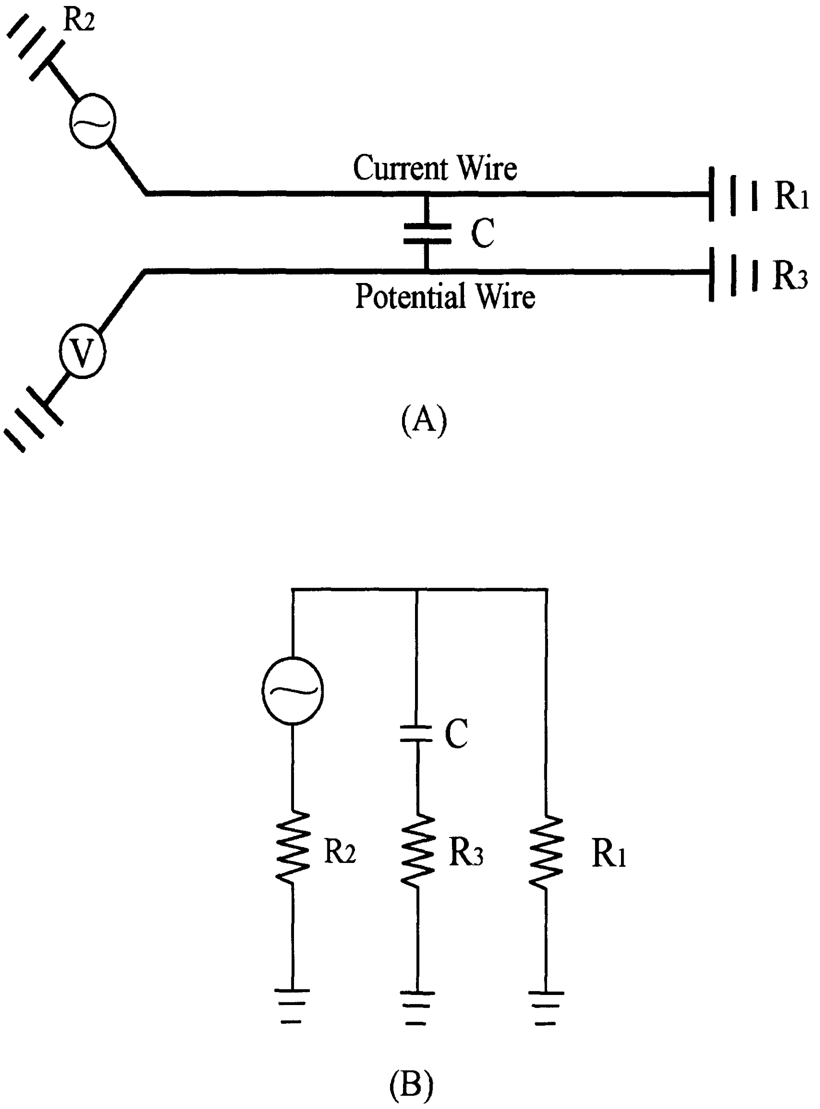

Figure 4.3 – Schematic diagram (A) and equivalent circuit (B) of capacitive couipling. C is the capacitance between the transmitting and receiving wires, R_1 and R_3 are the contact resistance of the current and potential electrodes respectively. The measured impedance due to coupling is the impedance calculated over the potential electrode R_3

4. Results

Time limitations have only allowed for data inversion at the two fundamental frequencies, .25 and .0625 hertz. Data are presented in two different forms, [1] as two dimensional panels each with its own scale and [2] as a three-dimensional volume characterized by slices in the depth plane. Volumetric data is obtained using the built-in Matlab function, *griddata3*. Data are linearly interpolated from the six panels to a three dimensional grid containing all boreholes. A three-dimensional interpolation is not as accurate as a full three-dimensional inversion, however is useful to help give a general idea of the distribution.

Figures 5.1 through 5.6 are the two-dimensional inversion results at both frequencies, data are presented as real and imaginary resistivity in ohm-meters, phase in milliradans and amplitude in ohm-meters. Detailed figure captions highlight the anomalous regions within each panel though a trend is noticeable throughout the panels. A phase anomaly is seen in the upper left corner of panels 1-2, 1-3, 1-4 and 2-3 at both frequencies (refer to phase plots of figures 5.1, 5.2, 5.2 and 5.4). Panels 1-2, 1-3 and 1-4 all have borehole 1 as the left edge, while panel 2-3 has borehole 2. The fact that the anomaly is witnessed from different boreholes takes credibility away from the notion that the anomaly is real and suggests that it may in fact be an inversion artifact.

A second region of interest is seen in panels 2-3 and 2-4 which both have borehole 2 as their left boundary. For both of these panels an imaginary resistivity anomaly is seen at depths of 17 to 25 meters on the left side of the panel. Values range considerably between both panels and frequencies, however its existence may suggest that this is an area of concern.

Panel 2-4 contains an anomalous region in both phase and imaginary resitvity. The elevated values appear at depths of 5 to 25 meters at both frequencies. However the magnitude of these values changes drastically between the two frequencies which is cause for concern. In theory, the differences between .25 and .0625 Hertz should not be very large perhaps indicating that the structure of this inversion is correct, but the inversion did not entirely finish.

Figures 5.7 through 5.10 are the three-dimensional interpolations of the two-dimensional panels. Descriptions are presented in figure captions and highlighted by dashed boxes. Refer to the imaginary resistivity plot on figure 5.8, a very large anomalous region is seen within panel 2-4 at all depths at .25 Hertz. However, as seen in figure 5.8, this anomaly is not found at the lower frequency, note that both plots are on the same scale. Also on figure 5.8, an imaginary resistivity anomaly is seen within panel 3-4 at depths less than 10 meters which is not seen at the higher frequency. This anomaly is highlighted by the presence of a dashed box around it.

In figure 5.9, phase plot of .25 Hertz, a strong anomaly at the surface is emanating from borehole 1 in all directions. It does not extend much below the surface and has very large values over 800 milliradians. The same anomaly is seen at .0625 Hertz in figure 5.10, however much less in magnitude.

.25 Hertz

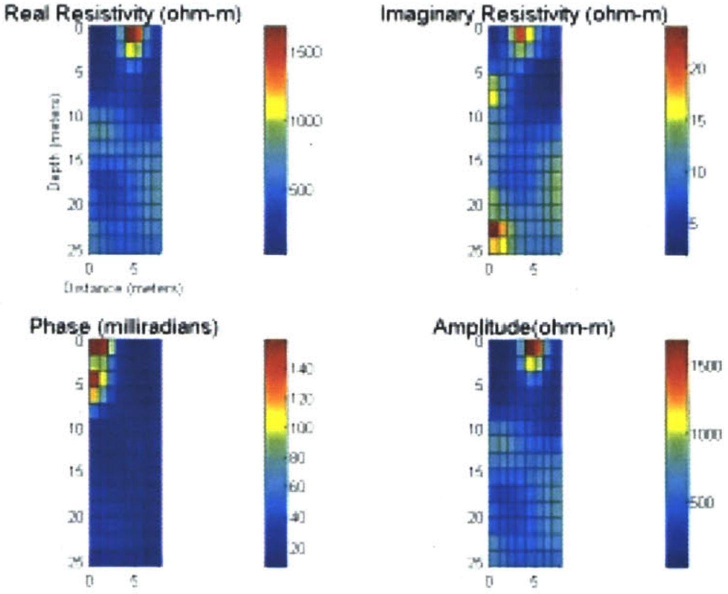

.0625 Hertz

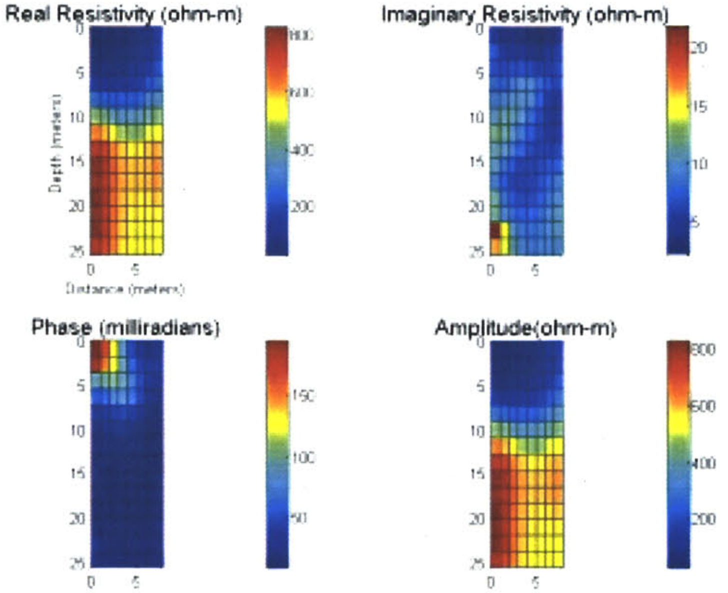

Figure 5.1 – Panel 1-2 inverted resitivity models at both frequencies. Phase and amplitude have been calculated from real and imaginary resitivity inversions. Two anomalies are seen within the panel, phase in the upper left corner and imaginary resistivity in the lower left corner. Note that all plots are not on the same scale.

.25 Hertz

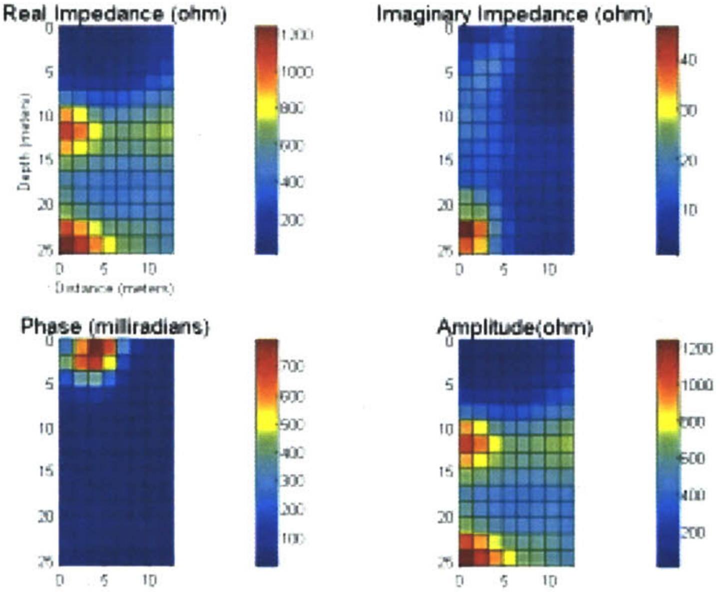

.0625 Hertz

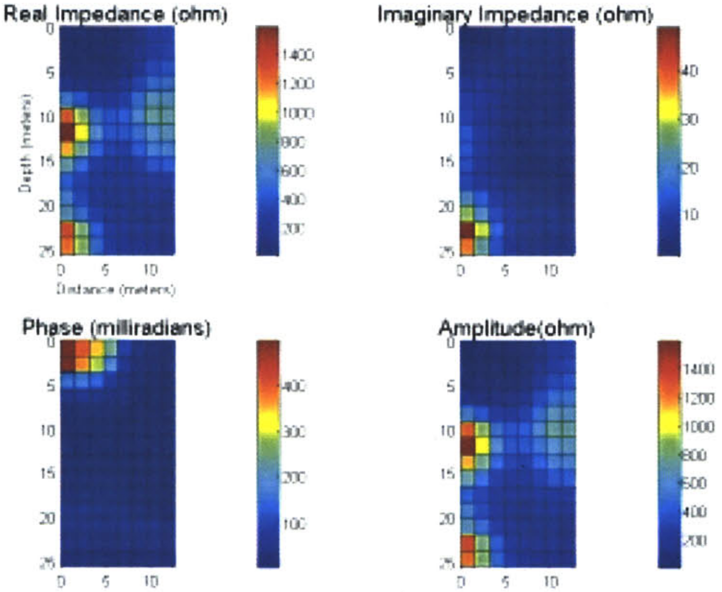

Figure 5.2 – Panel 1-3 inverted resitivity models at both frequencies. Phase and amplitude have been calculated from real and imaginary resitivity inversions. Two anomalies are seen within the panel, phase in the upper left corner and imaginary resistivity in the lower left. Note that all plots are not on the same scale.

.25 Hertz

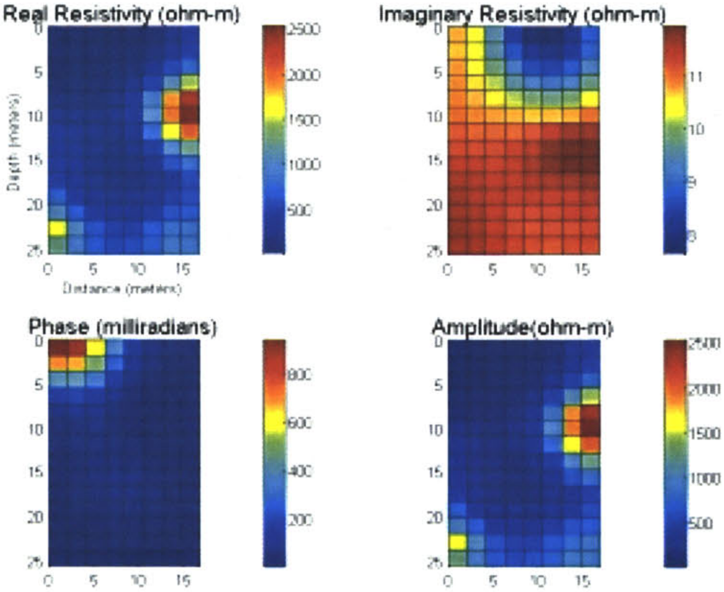

.0625 Hertz

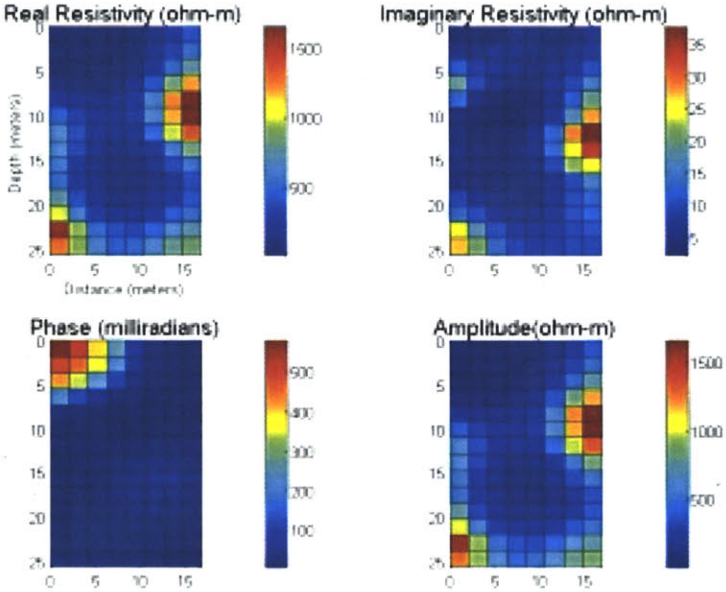

Figure 5.3 – Panel 1-4 inverted resitivity models at both frequencies. Phase and amplitude have been calculated from real and imaginary resitivity inversions. Two anomalies are seen within the panel; phase in the upper left corner and imaginary resistivity in the central right area. Note that all plots are not on the same scale.

.25 Hertz

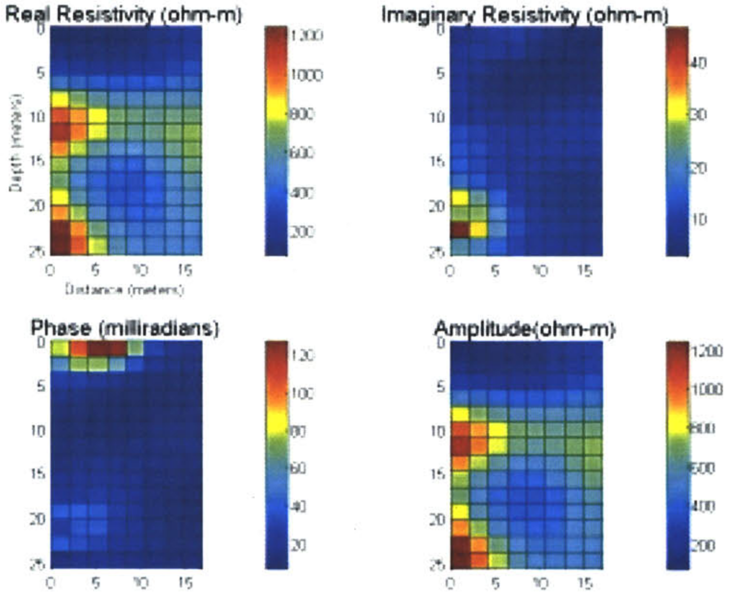

.0625 Hertz

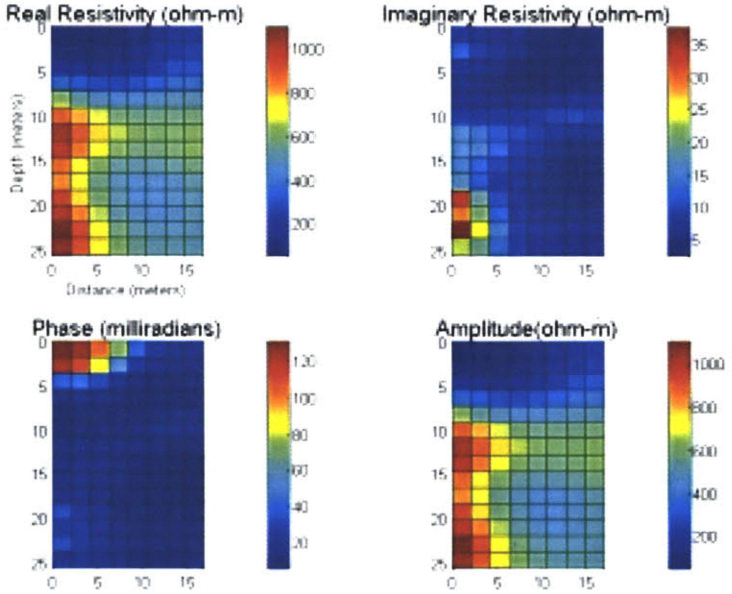

Figure 5.4 – Panel 2-3 inverted resitivity models at both frequencies. Phase and amplitude have been calculated from real and imaginary resitivity inversions. Two anomalies of interest are seen within the panel; phase in the upper left corner and imaginary resistivity in the central right area. Note that all plots are not on the same scale.

.25 Hertz

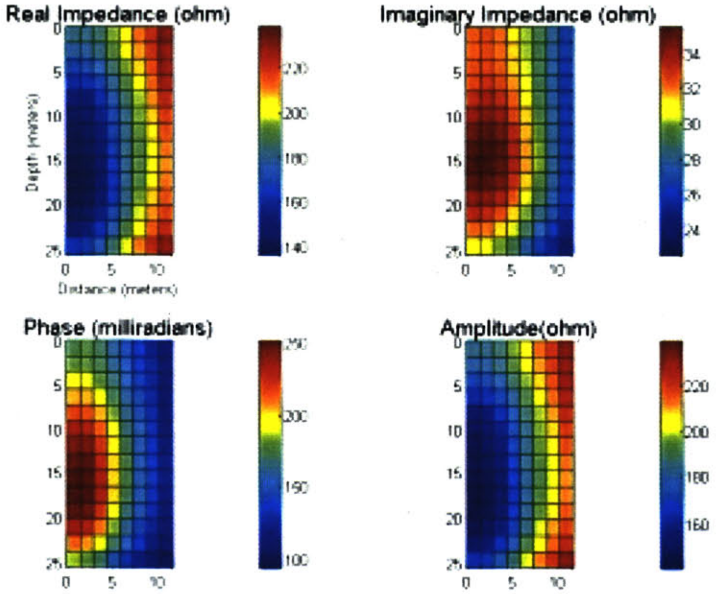

.0625 Hertz

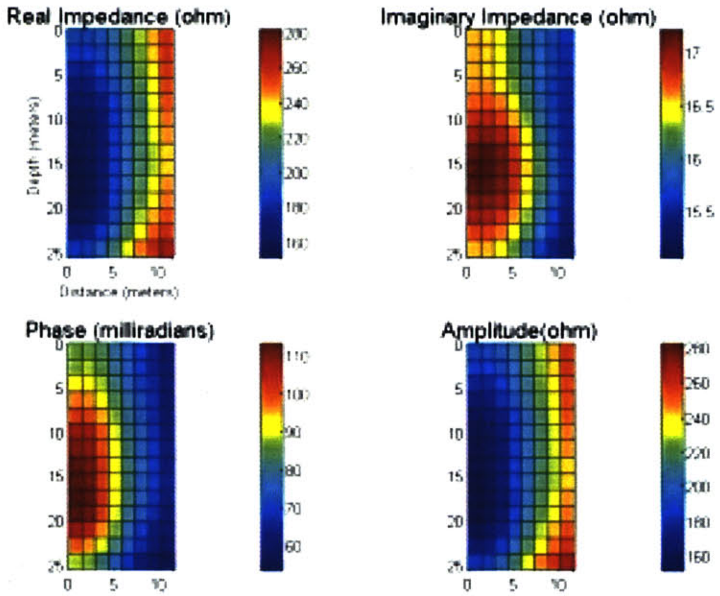

Figure 5.5 – Panel 2-4 inverted resitivity models at both frequencies. Phase and amplitude have been calculated from real and imaginary resitivity inversions. Phase and imaginary resistivity are very similar for the two panels. The overall structure of the inversions between the frequencies is similar however different values may suggest that the inversion has not completed.

.25 Hertz

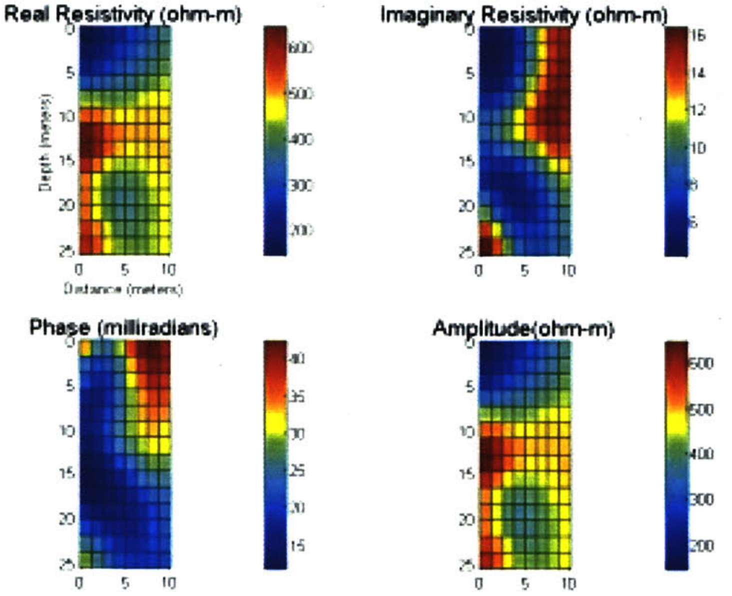

.0625 Hertz

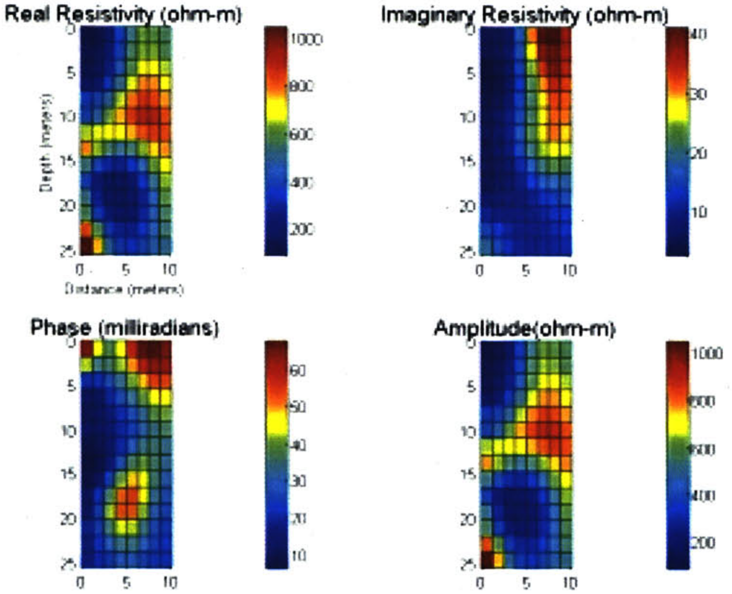

Figure 5.6 – Panel 3-4 inverted resitivity models at both frequencies. Phase and amplitude have been calculated from real and imaginary resitivity inversions. A clear imaginary resistivity anomaly runs from the top of borehole 4 (right side) to half way down the panel. Phase is also very busy within this panel as two regions are seen to be anomalous. A moderately valued anomaly within the bottom center of the panel and the entire top 5 meters of the panel show changes relative to background.

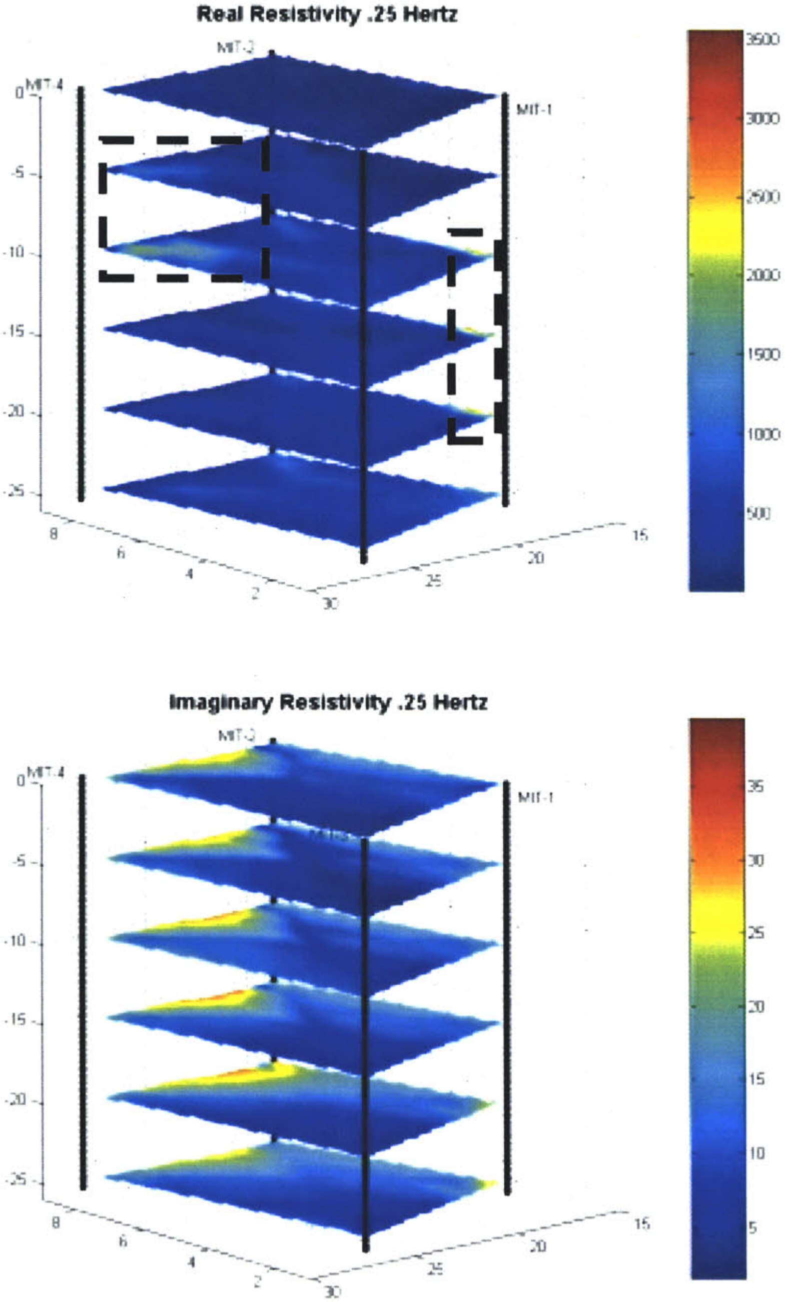

Figure 5.7 – Three-dimensional rendering of the six two dimensional panels. Both real resistivity and imaginary resistivity have units of ohm-meters. A clear imaginary resistivity anomaly is seen within panel 2-4 at all depths. Real resistivity exhibits anomalous values at two places highlighted by the dashed boxes. A moderate anomaly at depths of 5 to 10 meters near borehole 4 and a very strong anomaly greater than 10 meters depth near borehole 1.

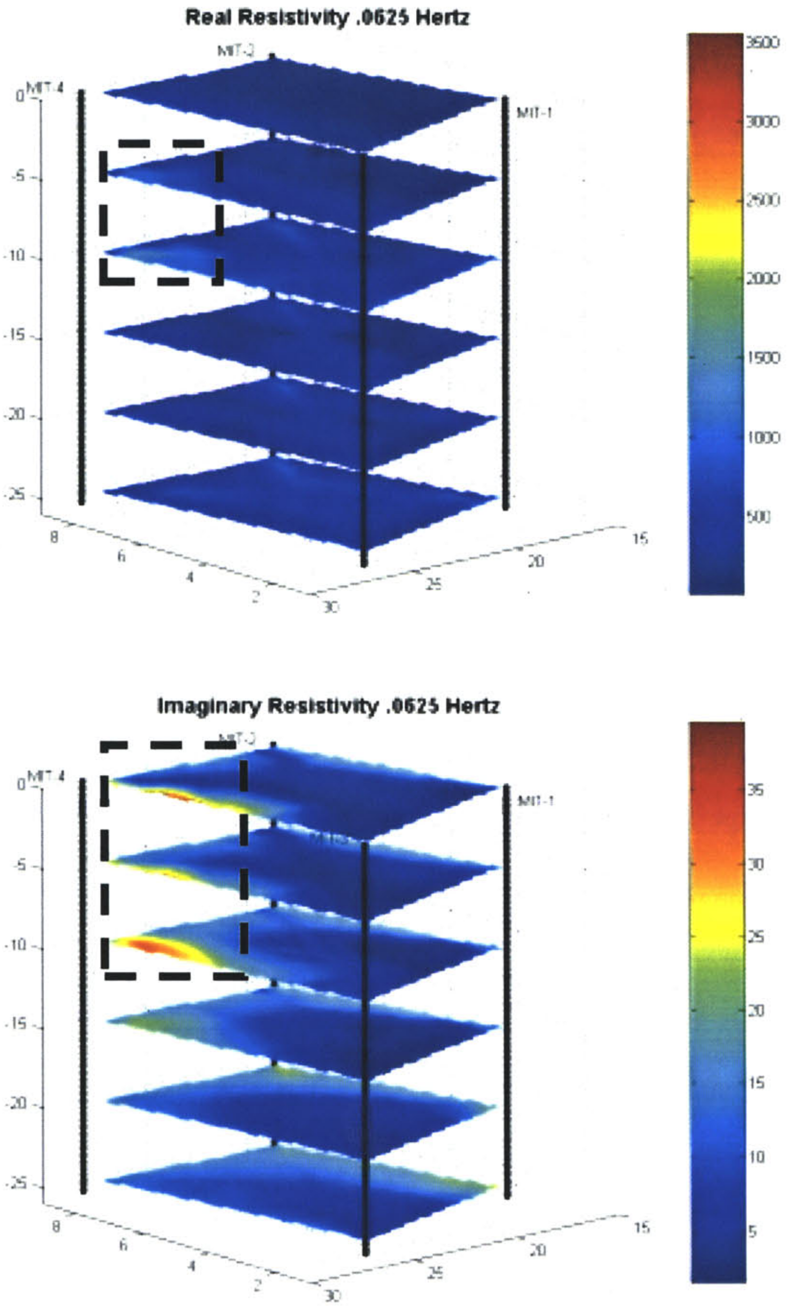

Figure 5.8 – Three-dimensional rendering of the six two dimensional panels. Both real resistivity and imaginary resistivity have units of ohm-meters. A clear imaginary resistivity anomaly is shown in the dashed box within panel 3-4 at depths less than 10 meters. The same anomalous value is seen in real resistivity near borehole 4, however much less in magnitude.

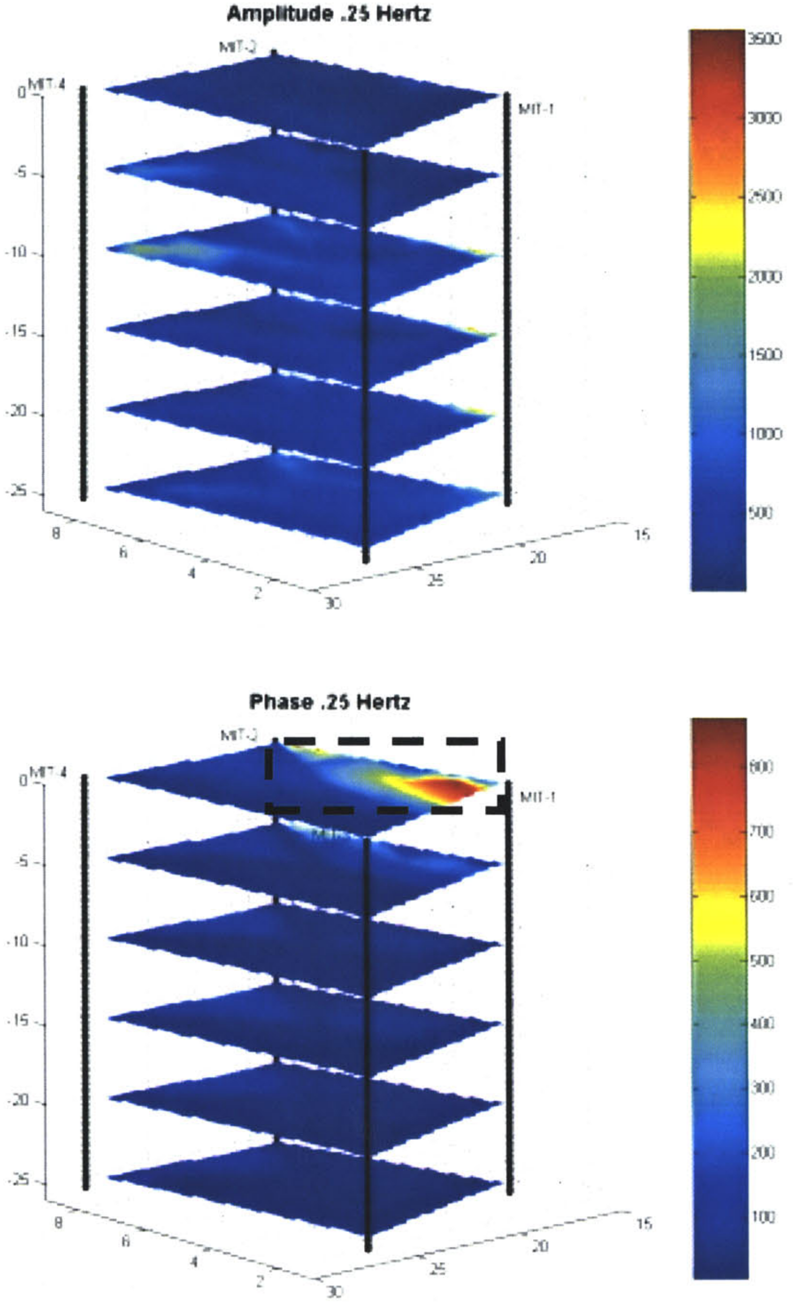

Figure 5.9 – Three-dimensional rendering of the six two dimensional panels. Amplitude has units of ohm-meters and phase has units of milliradians. As expected, amplitude exhibits the same characteristics as real resistivity at this frequency, for this reason it will not be discussed. Phase exhibits strong anomalous values near the surface emanating from borehole 1 in all directions, seen in dashed box.

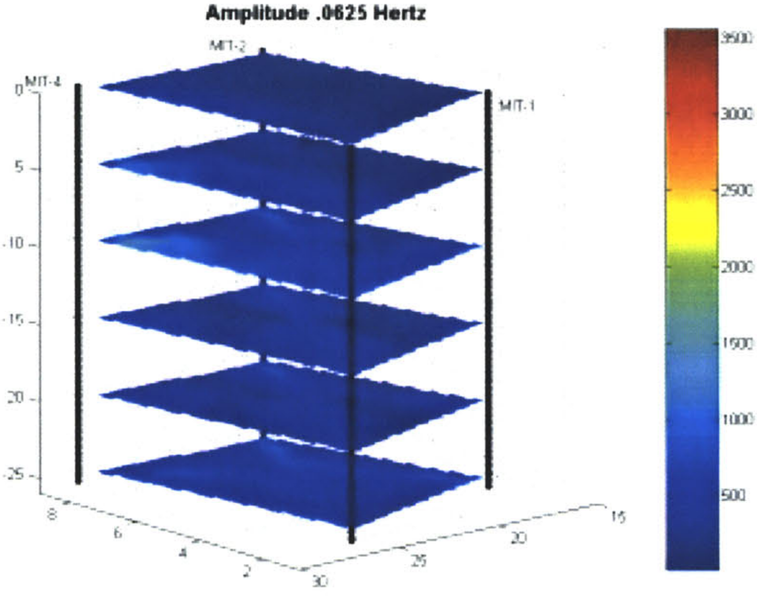

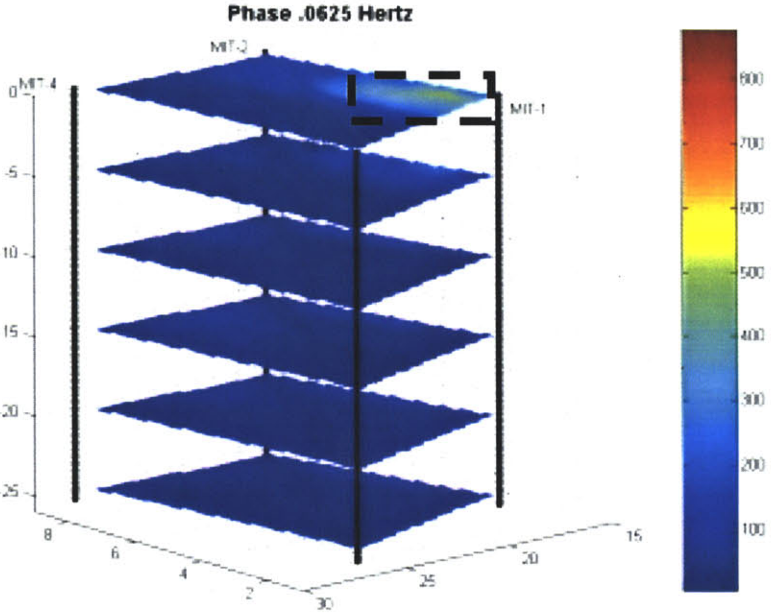

Figure 5.10 – Three-dimensional rendering of the six two dimensional panels. Amplitude has units of ohm-meters and phase has units of milliradians. Again as expected, amplitude exhibits the same characteristics as real resistivity at this frequency, for this reason it will not be discussed. Similarly to the higher frequency, phase exhibits anomalous values near the surface emanating from borehole 1, seen in dashed box.

5. Interpretation

The interpretation of SIP data and IP data in general, can be very ambiguous and difficult considering the possibilities of error creeping into the data, mostly through noise. Processing techniques have been developed to remove some forms of noise; however, this is not the case for all sources. Misinterpretation can also occur due to data inversion problems and the non-uniqueness associated with this process. For these reasons it is important interpretation is performed in the light of all possible noise sources and consideration of the fact that other steps may be necessary to effectively delineate contaminants.

To help with interpretation, data from a previous MIT field excursion at the Savannah River Site is introduced. Data was collected at five frequencies between MES-2 and MES-4 (refer to figure 1.1). A section of the correct subsurface contaminant distribution as determined by chemical analyses is shown in figure 6.1. The contaminated region consists of a small block at 10 to 13 meters depth in the right-center of the panel. Concentrations reach a maximum of 1.5 ppmv within this anomaly. With this knowledge it is now appropriate to plot the IP data in its many forms and determine which physical parameter best characterizes the contaminated region. Physical parameters include: real and imaginary conductivity, real and imaginary resistivity, phase, amplitude, percent frequency effect, metal conduction factor, resistivity and conductivity differences and ratios, amplitude ratio and phase difference. These results are shown in figures 6.2 through 6.7. The white box on each of the figures corresponds to the contaminated region in figure 6.1.

Results show that phase, figure 6.3, and imaginary resistivity, figure 6.2, highlight the contaminated region more effectively than other parameters. This will limit our discussion of anomalous regions within the MIT wells to the phase and imaginary resistivity distribution.

Please refer to figures 5.7 through 5.10, the three-dimensional interpolations of the two dimensional panels. This discussion only pertains to phase and imaginary resistivity, where three anomalous regions are of interest between the two frequencies. Imaginary resistivity on figure 5.7 shows an anomalous region within panel 2-4. Imaginary resistivity values exceed 35 ohm-meters when the anomaly reaches its maximum at 15 meters depth. Two main problems with this data disqualify it from being considered contamination: [1] the amount of usable data from panel 2-4 is very small at high frequencies, refer to figure 3.1, this suggests that data quality is very poor, and a more rigorous data reduction scheme may help alleviate these errors, and [2] the anomaly spans the entire height and width of the borehole, not many background values are seen within this region, this is a sign that the inversion result is not reliable.

The next region of interest is seen in the imaginary resistivity plot on figure 5.8 and is surrounded by a black dashed box. This anomaly is very likely to be contamination because it is in close proximity to the discharge pipe (next to borehole 4 within panel 2-4). The major argument against this anomaly is that it does not show up at both frequencies.

The last region of interest appears next to borehole 1 at both frequencies in the phase plots. This anomaly is very strong at the surface and does not extend past a depth of 5 meters. However it does not appear to be contaminant for two reasons: [1] the very large phase values approaching 800 milliradians and [2] its location does not correspond well with the location of the discharge pipe. The large values are indicative of the presence of metal and exceed expected values for contaminant.

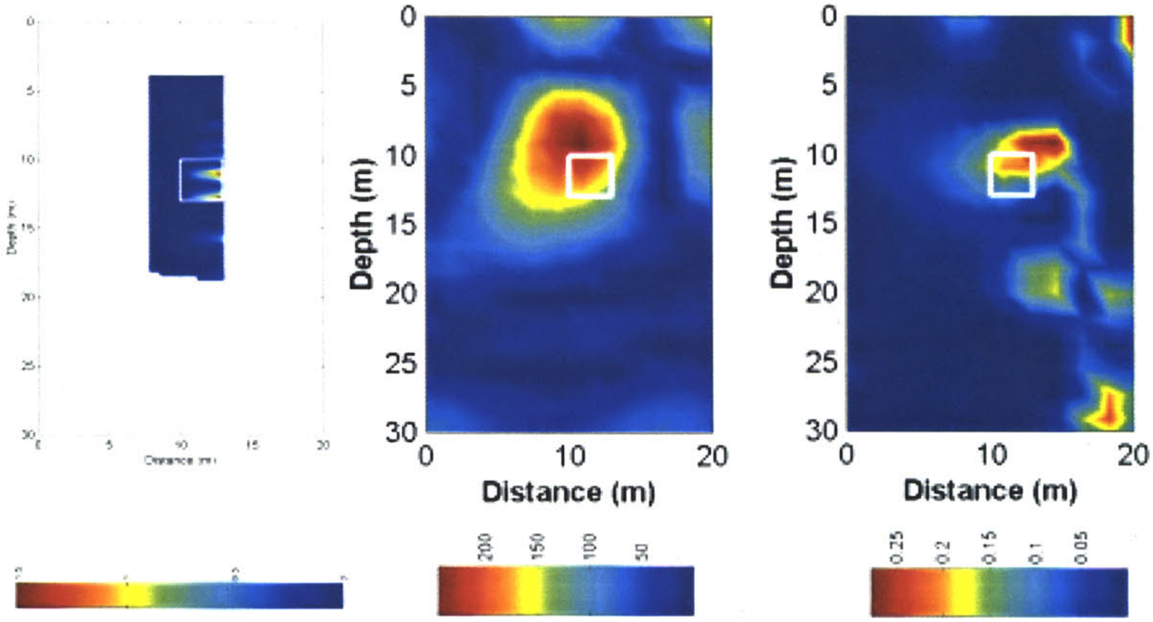

PCE-IP ground truth comparison at the A-14 Outfall

Figure 6.1 - Comparison of the ground-truth PCE anomaly (**a**), the ERL's SIP anomaly (**b**), and the ERL's TDIP anomaly (**c**). Panel **a** has been generated by taking a slice along the MES-2/MES-4 panel from the volumetric PCE concentration (interpolated from the CRS series of boreholes, taken during the FY01 ground-truth exercise). Panels **b** and **c** are the ERL's inversion results along the MES-2/MES-4 panel. MES-4 is located on the right-hand side of all three panels. (Morgan, 2001)

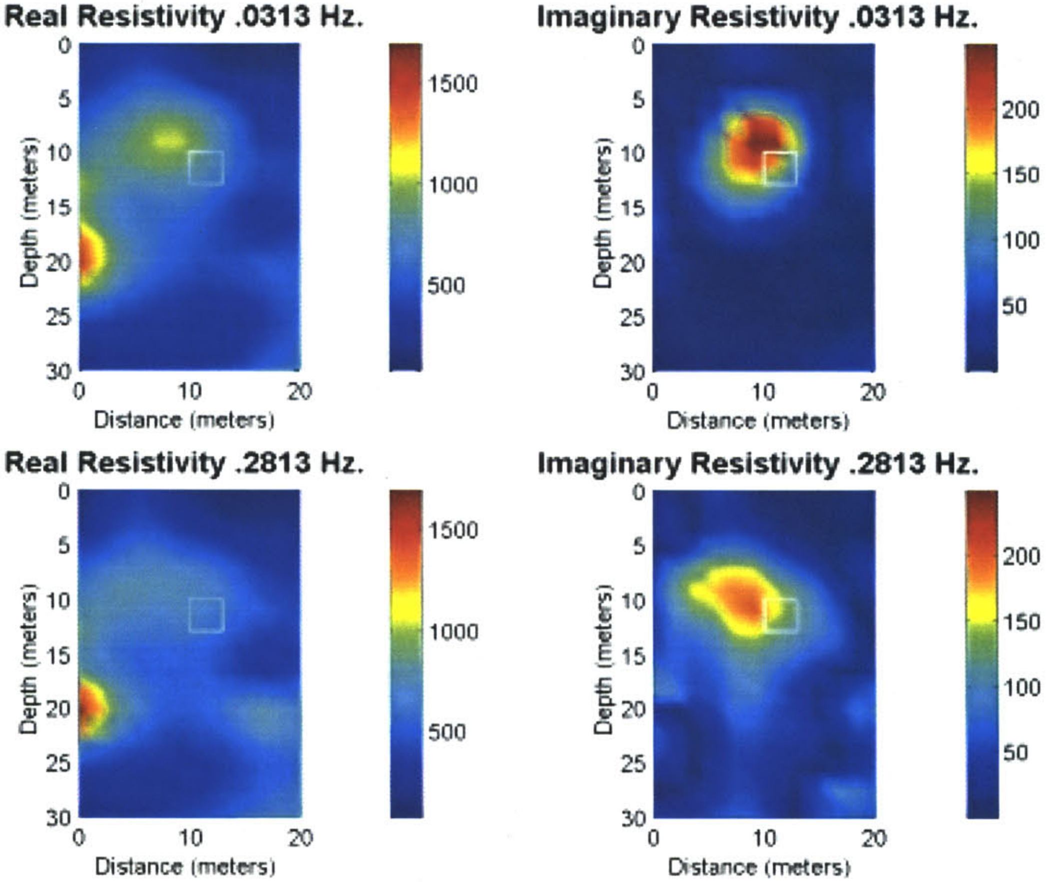

Real Resistivity .0313 Hz.

Imaginary Resistivity .0313 Hz.

Real Resistivity .2813 Hz.

Imaginary Resistivity .2813 Hz.

Figure 6.2 – Real resistivity (ohm-meters) and imaginary resistivity (ohm-meters) at two frequencies. Data from MIT 2001 SRS campaign. White box is location of anomaly as determined by chemical results in Jackson et al. (2000).

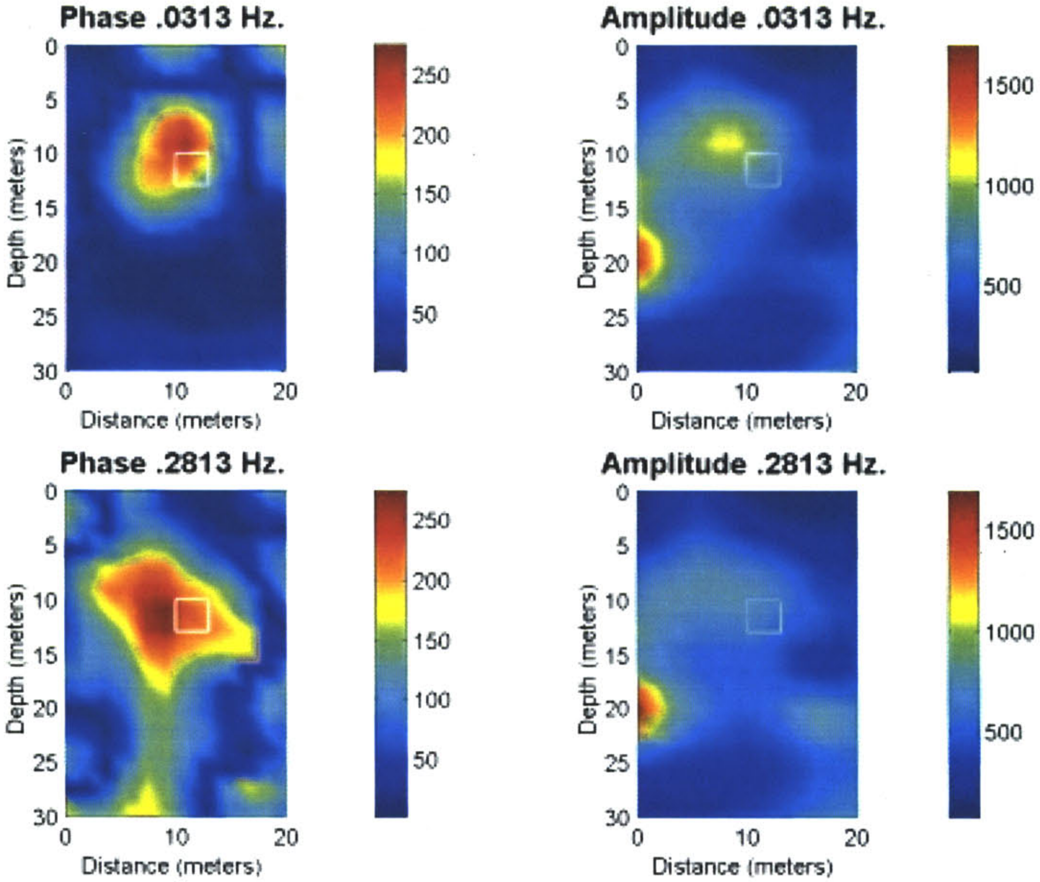

Phase .0313 Hz.

Amplitude .0313 Hz.

Phase .2813 Hz.

Amplitude .2813 Hz.

Figure 6.3 - Phase (milliradians) and amplitude (ohm-meters) at two frequencies. Data from MIT 2001 SRS campaign. White box is location of anomaly as determined by chemical results in Jackson et al. (2000).

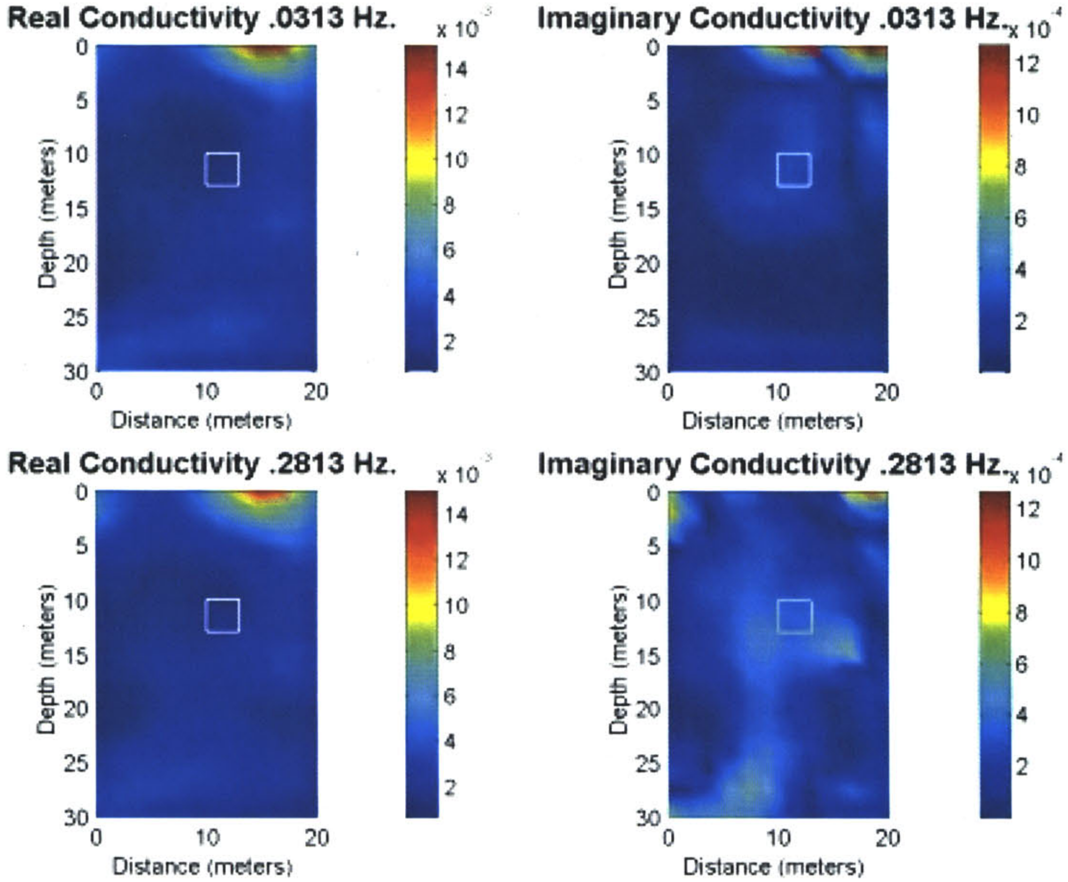

Figure 6.4 - Real conductivity (mhos/meter) and imaginary conductivity (mhos/meter) at two frequencies. Data from MIT 2001 SRS campaign. White box is location of anomaly as determined by chemical results in Jackson et al. (2000).

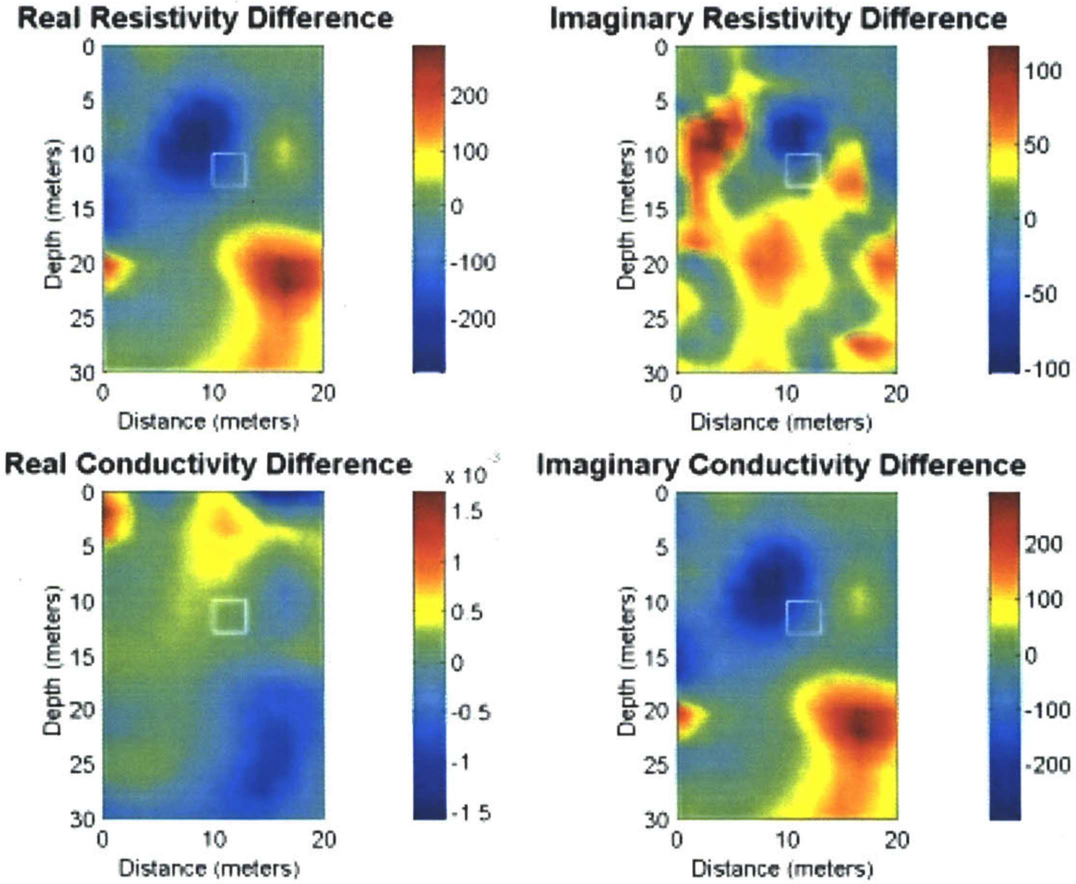

Figure 6.5 – Difference plots of real and imaginary resistivity and conductivity (.2138 Hz. - .0313 Hz.). Data from MIT 2001 SRS campaign. White box is location of anomaly as determined by chemical results in Jackson et al. (2000).

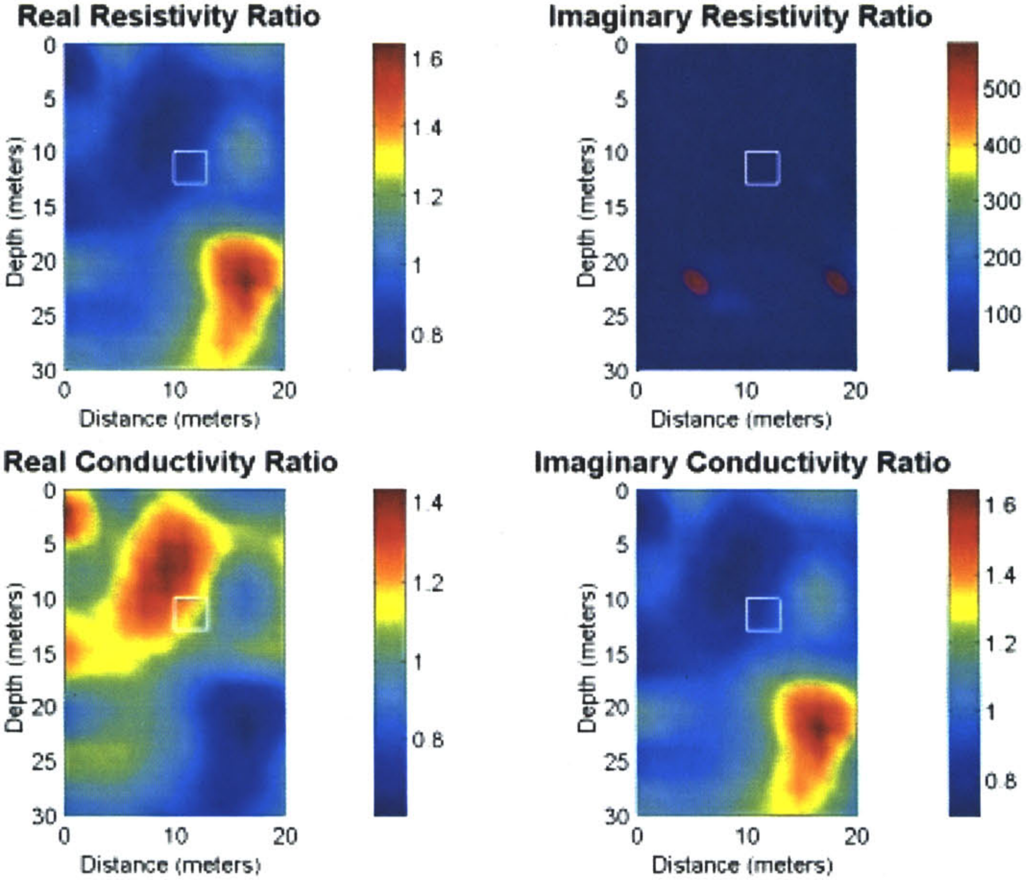

Figure 6.6 – Ratio plots of real and imaginary resistivity and conductivity (.2138 Hz./.0313 Hz.). Data from MIT 2001 SRS campaign. White box is location of anomaly as determined by chemical results in Jackson et al. (2000).

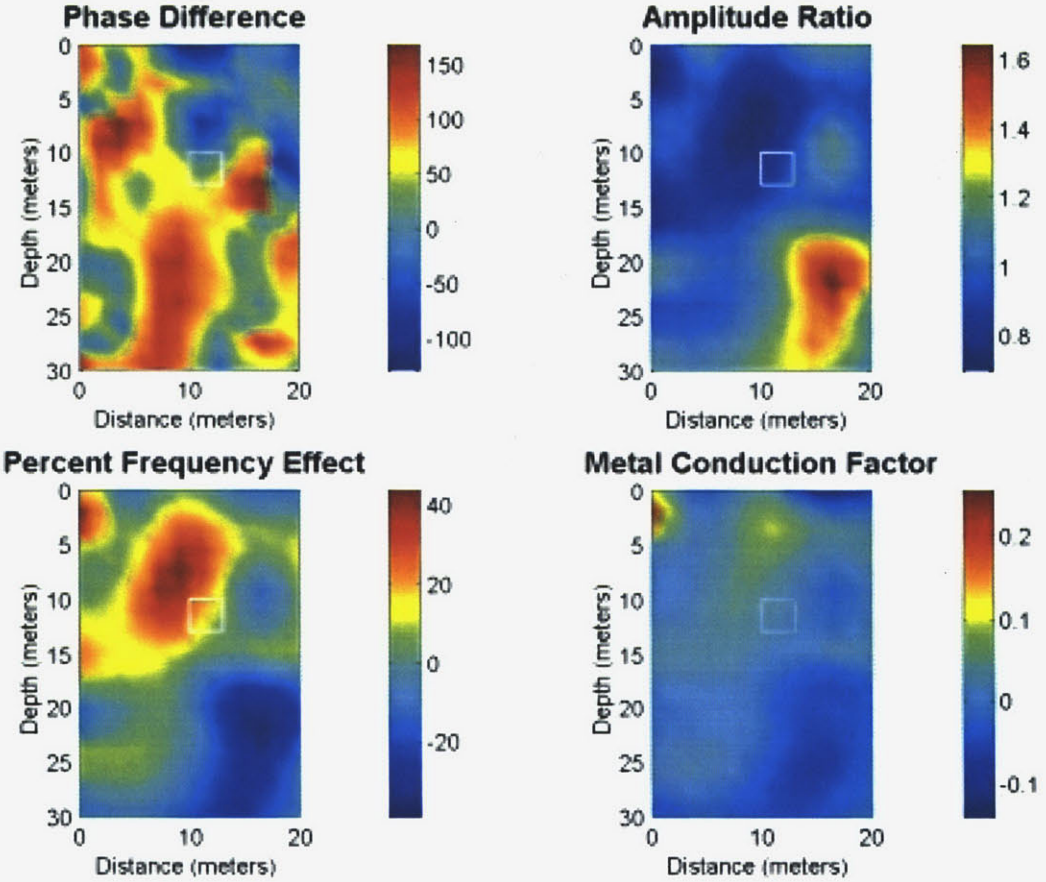

Figure 6.7 – Phase difference plot (.2138 Hz. - .0313 Hz.), amplitude ratio plot (.2138 Hz. / .0313 Hz.), percent frequency effect (%) and metal conduction factor. Data from MIT 2001 SRS campaign. White box is location of anomaly as determined by chemical results in Jackson et al. (2000).

6. Conclusion

The ability of SIP to detect the presence of organic contamination is well known and documented. Difficulties arise in filtering out the many sources of noise and interpreting data in the context of noise sources and errors arising due to non-unique inversions. However noise can be minimized through the use of proper equipment, consideration of site conditions and data filtering schemes.

This study exhibited the use of SIP for detecting dense non-aqueous phase liquids at the Savanna River Site, SC. The Zonge GDP-32 II multi function receiver was used for data collection. Non-polarizing Ag-AgCl electrodes used for potential measurements reduced the inherent noise of the electrode. Collected data was converted to real and imaginary impedance and inverted for model parameters using a real domain resistivity inverse code.

The main objective of this study was not met as no clear zone of contaminant could be delineated with this method. However to fulfill the entire scope of the project, three locations are recommended to drill ground truthing wells. Their locations are presented in figure 7.1. GT-1 is located between MIT-3 and MIT-4 at a distance of 5 meters from MIT-3. If contaminant is present it will be located above five meters in depth within this region. GT-2 is located near borehole 1 and is intended to show that these high anomaly values are in fact not indicative of contaminant but caused by the presence of other materials. Lastly, GT-3 is located near borehole 3 within panel 1-3 and is intended to show that SIP is able to not find contaminant.

Future work using SIP for contaminant delineation requires formulation of the inductive coupling effects in the borehole geometry and the formulation of an appropriate correction scheme. Questions regarding the effects of equipment grounding on measurements are very serious and should be addressed and resolved within the near future. More laboratory studies should be initiated to further current knowledge about contaminant affect on SIP, and also to clarify the effects of contaminant concentration.

Ground Truthing Wells

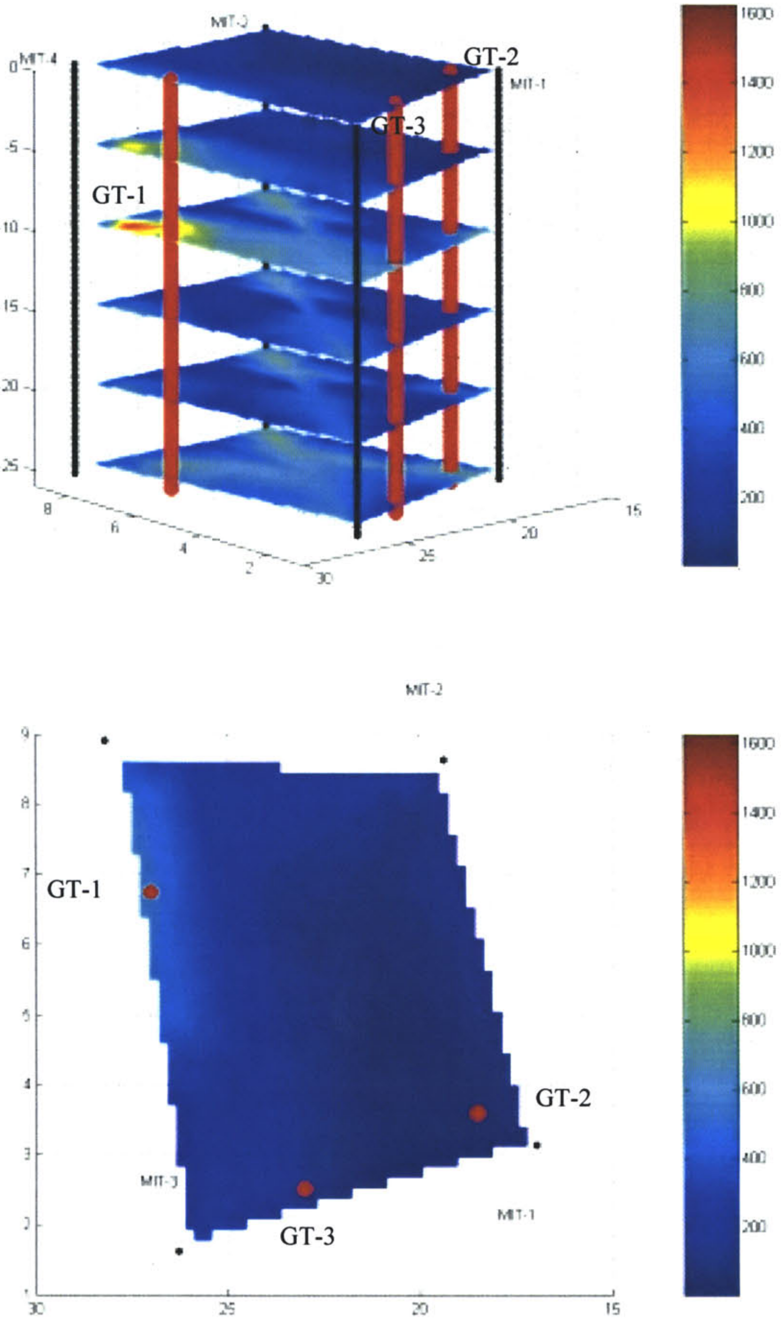

Figure 7.1 – Locations of three ground truthing wells relative to the locations of the wells used in this study. GT-1 is possibly contaminated while GT-2 and GT-3 should not produce any contaminated material.

References

Jackson, D. G., Hyde, W. K., Rossabi, J., Riha, B. D. (2000), *Characterization Activities to Determine the Extent of DNAPL in the Vadose Zone at the A-014 Outfall of A/M Area*, WSRC-RP-99-00569, DOE Contract No. DE-AC09-96SR18500.

Johnson, C.D., Dawson, C.B., Belaval, Marcel, and Lane, J.W., Jr., (2002a), An integrated surface-geophysical investigation of the University of Connecticut landfill, Storrs, Connecticut -- 2000: U.S. Geological Survey, Water Resources Investigations Report 02-4008, 39 p.

Johnson, C.D., Haeni, F.P., Lane, J.W., and White, E.A. (2002b), *Borehole-geophysical investigation of the University of Connecticut landfill*, Storrs, Connecticut: U.S. Geological Survey, Water Resources Investigations Report 01-4033, 187 p.

Lane, J.W., Jr., Buursink, M.L., Haeni, F.P., and Versteeg, R.J., 2000, *Evaluation of ground-penetrating radar to detect free-phase hydrocarbons in fractured rocks-results of numerical modeling and physical experiments*, Groundwater, v.38 no.6, p. 929-938.

Lesmes, D. P., and Frye, K. F., 2001, *The influence of pore fluid chemistry on the complex conductivity and induced polarization responses of Berea sandstone*, Jour. Geophys. Res., 106, 4079-4090

Madden, T.R., Cantwell, T. (1967) Induced *Polarizatin, a review*, in Mining Geophysics, v. II, Soc. Exp. Geophys., 373-400

Marshall, D.J. and Madden, T.R., (1959) *Induced Polarization: A study of its causes.* Geophysics, 24, 790-816.

McKinley, K.S. (2003), *Nonlinear Complex Resistivity to Investigate Clay-Organic Reactions at the Savannah River Site, South Carolina*, unpublished M.S. thesis, Colorado School of Mines, 90 pp.

Millett, F. B. (1967), *Electromagnetic Coupling of Collinear Dipoles on a Uniform Half Space*, Mining Geophysics 2, Tulsa, SEG, 401-419.

Morgan, F.D. (2001), *A Spectral Induced Polarization Survey to Delineate Subsurface Contamination for the U.S. Department of Energy: A-014 Outfall, Savannah River Site, S.C.*, Report to the U.S. Department of Energy, 126 pp.

Olhoeft, G. (1992), *Geophysical Detection of Hydrocarbon and Organic Chemical Contamination*, SAGEEP Proceedings, Oakbrook, IL, 587-594.

Petiau, G., and Dupis, A. (1980), *Noise, Temperature Coefficient, and Long Time Stability of Electrodes for Telluric Observations*, Geophysical Prospecting 29, 792-804.

Petiau, G. (2000), *Second Generation of Lead-lead Chloride Electrodes for Geophysical Applications*, Pure and Applied Geophysics 157, 357-382.

Powers, C.J., Wilson, Joanna, Haeni, F.P., and Johnson, C.D., 1999, *Surface-geophysical investigation of the University of Connecticut landfill, Storrs, Connecticut*, U.S. Geological Survey Water-Resources Investigations Report 99-4211, 34 p.

Slater, L. D., Lesmes, D. L., The Induced Polarization Method,

Sumner, J. S. (1976), *Principles of Induced Polarization for Geophysical Exploration.* Elsevier Scientific, Amsterdam, 277pp.

Wait, J. R. (1959), *Overvoltage Research and Geophysical Applications*, New York, Pergamon Press, 158. p.

Ward, S. H. (1990), *Resistivity and Induced Polarization Methods*, in Ward, S. H., Geotechnical and Environmental Geophysics: Volume I, Review and Tutorial, Soc. Explor. Geophys., 147-190.

Williams, J. H., Lane, J. W., Singha, K., and Haeni, F. P., 2002, *Application of advanced geophysical logging methods in the characterization of a fractured-sedimentary bedrock aquifer, Ventura County, California:* U. S. Geological Survey Water-Resources Investigations Report 00-4083, 28p.

Vandiver, A. (1998), *Analysis of the Effects of Inductive Coupling in Induced-Polarization Surveys of Environmental Contaminants*, unpublished B.S. thesis, Massachusetts Institute of Technology, 18 pages.

Vangelas, K. M. (2000), *Summary and Status of DNAPL Characterization and Remediation Activities in the A/M Area, Savannah River Site*, WSRC-RP-2001-00171, DOE Contract No. DE-AC09-96-SR18500.

Vanhala, H., Soininen, H., Kukkonen, I. (1992), *Detecting Organic Chemical Contaminants by Spectral Induced Polarization Method in Glacial Till Environment*, Geophysics 57, 1014-1017.

Appendix

A. Equipment

Zonge Geophysical Equipment

A Zonge GDP-32 II multifunction receiver functioning in the complex resistivity mode was used for data collection. The GDP-32 II is a sixteen channel receiver that is expandable by the addition of the Zonge MX-30, 30 channel signal transmitting boxes. All current and potential electrodes were connected through both MX-30 boxes in an effort to avoid the mistakes and confusion that may occur when switching wires during a survey. The Zonge ZPB-600 power booster was not necessary in the field because injected currents were very small and could easily run off two 12 volt batteries in series. Coupled with the batteries and receiver is the Zonge ZT-30 EM/Resistivity transmitter, capable of inputting both frequency and time domain current into the earth, however, lack of regulation requires that the current be monitored. Figure A.1 is a schematic of equipment setup in the field and figure A.2 is a photograph of the equipment at the site. All equipment except two 12 volt batteries was housed in the rear of a minivan during data collection periods, this allowed easy access while protecting the equipment from inclement weather.

The GDP-32 II receiver was continuously run off of a laptop computer and any changes necessary for the receiver were programmed through the computer. Periodically this setup caused the receiver to freeze, however freezes did not result in data loss. The computer interface also facilitated easy transfer of the data collection schedule which the GDP required to run. Schedule files are sequences of commands which the receiver uses to identify the correct pairs of electrodes for current injection and potential measurements. A total of six schedule files were written each corresponding with a particular two-dimensional data panel.

A block from a typical schedule is shown in figure A.3; the transmitting electrodes are box-1 channels 1 and 2, while the potential measurements will take place in box-2 for all the channel pairs listed. Each of the commands within the schedule corresponds to a set of channels on the pair of MX-30 boxes. This configuration remained constant for the entire week of data collection to ensure that data from all panels could be easily compared and converted to other formats. A very simple data collection scheme was employed which minimized collection time while maximizing the amount of relevant data collected. Within each panel all possible permutations of the 14 borehole current electrodes were transmitted, and also each borehole was paired with the surface electrode. This gives a total of 63 current sources per panel. Potential measurements were all made relative to the top electrode in borehole MIT-1, yielding 27 measurements per current source. Data was collected for the first five odd harmonics of ¼ and 1/16 hertz.

Porous Pot Electrodes

Voltage measurement of the earth is a very sensitive process that is subject to noise contamination from many sources including polarization, electronic/electrolytic potentials, time stabilization and temperature stabilization. All of these factors can combine to possibly drown out the signal that the electrode is trying to detect, which is usually in the millivolt to volt range. In light of all of this information, the Ag-AgCl electrode was chosen because of its noise limiting potential with respect to the previously described sources, especially its inability to become polarized. Also, Petiau and Dupis (1980) found that Ag-AgCl electrodes equilibrate in one-half to one hour depending on the type of material in which the electrode is nested and telluric effects.

For salt-metal coupled electrodes such as the Ag-AgCl electrode used in this experiment, temperature stabilization is examined by looking at the Nernst equation.

$$E = \frac{RT}{nF} \ln \frac{\{M^{+n}\}}{\{M^{+n}\}_{eq}}$$

where:

R = ideal gas law constant
T = temperature
n = metal valency
F = Faraday constant
$\{M^{+n}\}$ = metal ion concentration
$\{M^{+n}\}_{eq}$ = equilibrium metal ion concentration at which potential goes to 0

A temperature coefficient is derived by taking the derivative of the potential with respect to temperature keeping in mind that concentration is a temperature dependent function. The resulting coefficient has units of μV/°C and is a measure of the voltage change with respect to a one degree change in temperature. Petiau and Dupis (1980) found that Ag-AgCl electrodes with a clay solution acting as the electrolyte have a temperature coefficient of -410 μV/°C which is average for metal-salt non-polarizing electrodes.

The design of the electrode is very important because of the physical constraints that are placed on its size and lifespan. For all 14 current and potential electrodes to fit down each borehole, the wires and electrodes were built to ensure a nominal size of less than three inches, the size of the borehole. The electrodes were also built with a plan of re-using them within the next year, which would only be possible if the electrolyte solution within the electrode was not depleted. This ultimately led to a design similar to the 'tube' electrode discussed in Petiau and Dupis (1980), with a modified interior based on the necessities of the electrode and our capabilities within the lab.

The electronic conductor of the electrode is a 99.9% pure silver mesh coated with Ag-Cl through electrolysis. The use of a mesh as opposed to a wire is to increase the overall surface area of the electronic conductor, decreasing the resistance at the electronic/electrolytic interface. Lead solder is used to connect the silver mesh to a piece of 12 gauge copper wire, this wire is continuously run from the electrode to the MX-30 boxes to minimize any resistance through that would occur at connections. The soldered connection is surrounded by an epoxy which keeps the connection waterproof and strong. Coors-Tek porous pots are epoxied inside 18 inch lengths of 1 inch PVC pipe, only the bottom of the pot makes contant with the earth. The electrolyte solution design is based on work from Petiau (2000) on the long term stability of an electrode for telluric measurements. A non-polarizing electrode placed on a damp medium, as is the case in these boreholes, causes a depletion of salt ions within the electrolyte through chemical diffusion across the semi-permeable porous pot. The time at which the saturation front reaches the silver mesh can be calculated from Ficks first law

$$\frac{dm}{dt} = -kS\frac{dC}{dt}$$

where:

m = mass of solute
S = cross sectional area of electrode
k = diffusion coefficient
C = concentration electrolyte
t = time

If the concentration gradient from the ground to the metal electrode is assumed to initially be constant, the following solution is reached for the time in question,

$$t_d = \left(\frac{2C_M - C_s - C_m}{C_s - C_m} \right) \frac{L^2}{4k}$$

where:

C_m = *maximum salt concentration*
C_s = *saturation concentration*
C_m = *minimum concentration outside of electrode*
k = diffusion coefficient of solution
L = length of electrode
(Petiau, 2000)

Completely saturating the electrolyte with salt is necessary to increase the life of the electrode, however adding additional non-dissolved salt increases its life even more by raising the value of C_M. For instance, if the salt solubility within the solvent is 1, then C_s is also 1 because it is necessary for the electrolyte to be saturated. The addition of 2 times the amount of non-dissolved salt after saturation of the electrolyte will yield a C_M value of 3.

A schematic of the electrodes is shown in figure A.4. The electrolytic solution was thickened by the addition of agar-agar powder, while the NaCl solution was boiled. Thickener is necessary to prevent liquid loss through the porous pot at a rate that exceeds ion diffusion in the case of dry material. Using the diffusion coefficient for our electrode, estimations can be made regarding it's lifespan; however, the coefficient may only be determined empirically requiring lengthy lab measurements. From Petiau and Dupis (1980) coefficient values of 50.6 mm^2/day for mud and 94.2 mm^2/day for liquid will be used as upper and lower bounds for the saturated agar solution. Calculating t_d using the known C_m value of zero gives an upper bound of 2 years and a lower bound of a little over 1 year.

Current Electrodes

Although not second in importance, current electrodes are required to be less precise than potential electrodes making fabrication quick and easy. One foot long copper tubes were connected to copper wire using copper brackets and nylon screws. The main concern when considering current electrodes is corrosion that might take place at the boundary of two metals when current is passing between them. For this reason, the only metal used on any part of the current electrode was copper, nylon screws were a good substitute because pure copper could not be found, and nylon is electrically insulating.

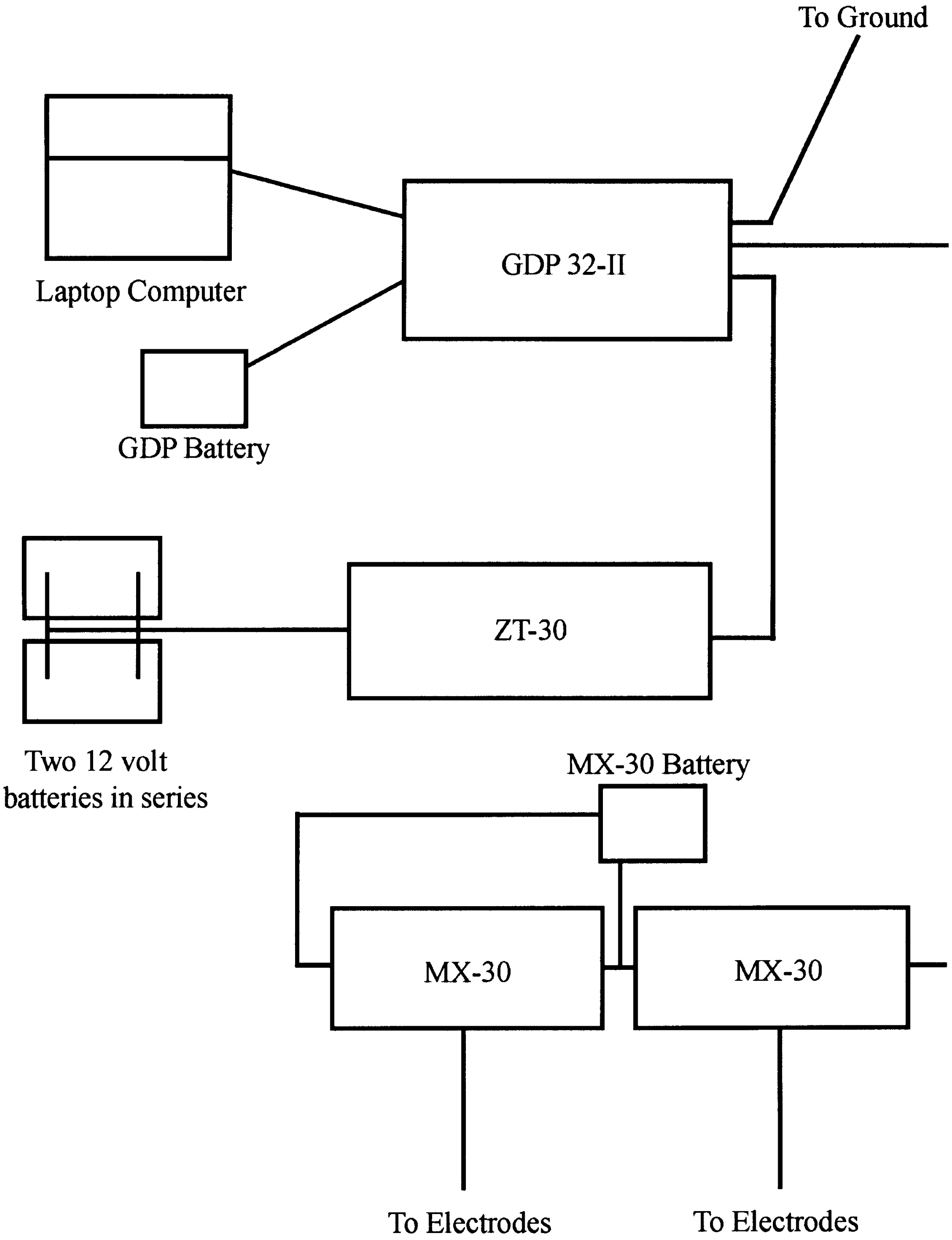

Figure A.1 – Schematic diagram of Zonge equipment setup in field, note that Zonge ZPB-600 power booster was not required in field and is not shown here.

Figure A.2 – Equipment at field site. Yellow boxes are MX-30 multichannel reveivers, white box is GDP-32 and gray box is ZT-30 power transmitter.

```
b2,TX-01,TX+08,b1,RX01,02,RX02,-02,RX01,03,RX03,-03,RX01,04,RX04,-
04,RX01,05,RX05,-05,RX01,06,RX06,-06,RX01,07,RX07,-07,RX01,08,RX08,-
08,RX01,09,RX09,-09,RX01,10,RX10,-10,RX01,11,RX11,-11,RX01,12,RX12,-
12,RX01,13,RX13,-13,RX01,14,RX14,-14
```

Figure A.3 – Typical data collection block from schedule file. For this particular block, box two electrode one and eight are the transmitting electrodes, all potential measurements are made relative to electrode one in box one.

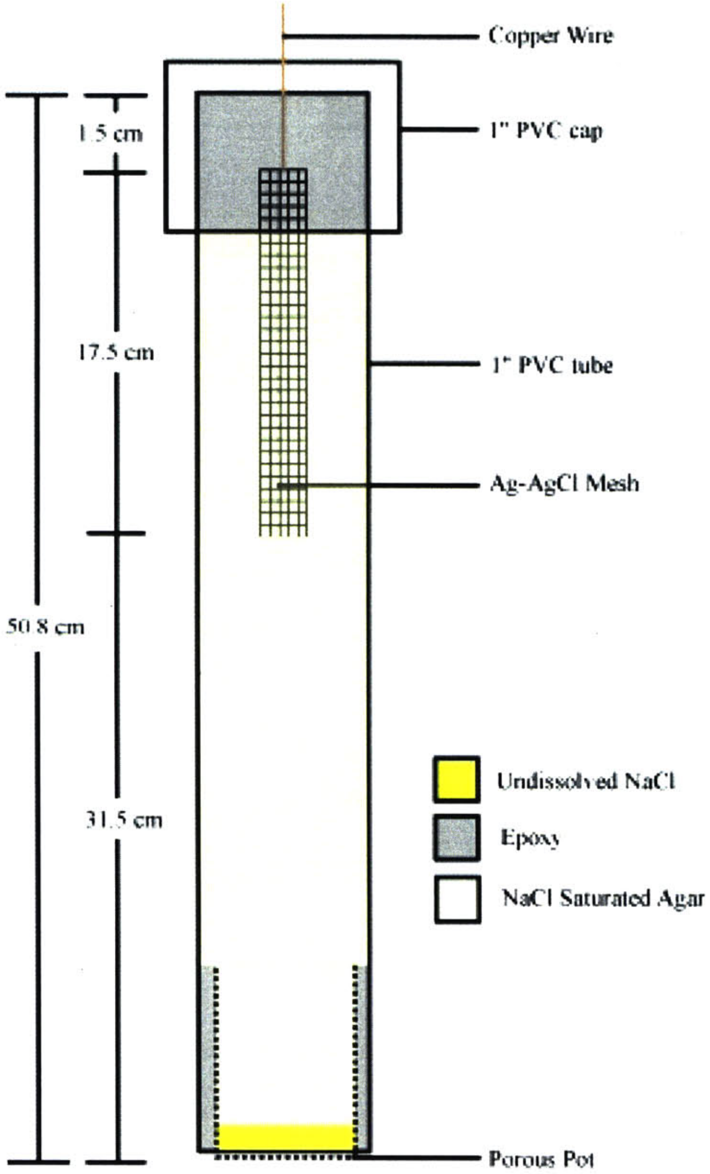

Figure A.4 – Schematic diagram of potential electrode. Note that drawing is not to scale.